

First Annual Report on Pulsed Thermal Tomography Nondestructive Evaluation of Additively Manufactured Reactor Materials and Components

*Pulsed Thermal Tomography Nondestructive Examination of Additively
Manufactured Reactor Materials and Components*

Nuclear Science and Engineering Division

About Argonne National Laboratory

Argonne is a U.S. Department of Energy laboratory managed by UChicago Argonne, LLC under contract DE-AC02-06CH11357. The Laboratory's main facility is outside Chicago, at 9700 South Cass Avenue, Argonne, Illinois 60439. For information about Argonne and its pioneering science and technology programs, see www.anl.gov.

Document availability

Online Access: U.S. Department of Energy (DOE) reports produced after 1991 and a growing number of pre-1991 documents are available free at OSTI.GOV (<http://www.osti.gov/>), a service of the U.S. Dept. of Energy's Office of Scientific and Technical Information

Reports not in digital format may be purchased by the public from the National Technical Information Service (NTIS):

U.S. Department of Commerce
National Technical Information Service
5301 Shawnee Rd
Alexandria, VA 22312
www.ntis.gov
Phone: (800) 553-NTIS (6847) or (703) 605-6000
Fax: (703) 605-6900
Email: **orders@ntis.gov**

Reports not in digital format are available to DOE and DOE contractors from the Office of Scientific and Technical Information (OSTI):

U.S. Department of Energy
Office of Scientific and Technical Information
P.O. Box 62
Oak Ridge, TN 37831-0062
www.osti.gov
Phone: (865) 576-8401
Fax: (865) 576-5728
Email: **reports@osti.gov**

Disclaimer

This report was prepared as an account of work sponsored by an agency of the United States Government. Neither the United States Government nor any agency thereof, nor UChicago Argonne, LLC, nor any of their employees or officers, makes any warranty, express or implied, or assumes any legal liability or responsibility for the accuracy, completeness, or usefulness of any information, apparatus, product, or process disclosed, or represents that its use would not infringe privately owned rights. Reference herein to any specific commercial product, process, or service by trade name, trademark, manufacturer, or otherwise, does not necessarily constitute or imply its endorsement, recommendation, or favoring by the United States Government or any agency thereof. The views and opinions of document authors expressed herein do not necessarily state or reflect those of the United States Government or any agency thereof, Argonne National Laboratory, or UChicago Argonne, LLC.

First Annual Report on Pulsed Thermal Tomography Nondestructive Evaluation of Additively Manufactured Reactor Materials and Components

*Pulsed Thermal Tomography Nondestructive Examination of Additively Manufactured
Reactor Materials and Components*

prepared by

Alexander Heifetz¹, Thomas W. Elmer¹, J.G. Sun¹, Tiffany Liu^{1,2}, Dmitry Shribak^{1,3}, Brian Saboriendo^{1,4}, Sasan Bakhtiari¹, Xin Zhang^{1,5}, Jafar Saniie⁵

¹Nuclear Science Engineering Division, Argonne National Laboratory

²Department of Physics, University of California at Berkeley, Berkeley, CA

³Department of Physics, University of Chicago, Chicago, IL

⁴Department of Physics, DePaul University, Chicago, IL

⁵Department of Electrical and Computer Engineering, Illinois Institute of Technology, Chicago, IL

September 30, 2019

Table of Contents

Table of Contents	1
List of Figures	2
List of Tables	5
Abstract	6
1. Introduction.....	8
1.1. Background.....	8
1.2. Overview.....	9
2. Modeling of Pulsed Thermal Tomography Performance	11
2.1. Mathematical basis of Pulsed Thermal Tomography	11
2.2. Validation of Effusivity reconstruction with COMSOL simulated data	13
2.3. Modeling of Internal Defect Detection.....	16
2.3.1. Basic Principles of Internal Flaw Detection with Thermal Tomography	16
2.3.2. Estimation of internal defect transverse size from COMSOL simulations	17
2.3.4. Defect reconstruction from COMSOL simulations	19
2.3.5. Estimated limits of defect size detection from COMSOL simulations.....	22
3. Imaging of Calibrated Defects in Metallic Specimens.....	26
3.1. PTT imaging of calibrated defects in high grade alloys	26
3.1.1. Development of flat bottom holes in Stainless Steel 316 and Inconel 718 plates	26
3.1.2. PTT imaging of Stainless Steel 316 plate with flat bottom holes.....	28
3.1.3. PTT imaging of Inconel 718 plate with flat bottom holes	32
3.2. PTT imaging of calibrated defects in lower grade alloys	35
3.2.1. Development of calibrated flat bottom holes Stainless Steel 304, Nickel 200 and Hastelloy C276 specimens	35
3.2.2. PTT imaging of Stainless Steel 304 plate with flat bottom holes.....	37
3.2.3. PTT imaging of Nickel 200 plate with flat bottom holes.....	38
3.2.4. PTT imaging of Hastelloy C276 plate with flat bottom holes.....	40
4. Imaging of Additively Manufactured Structures with Complex Geometry	42
4.1. Pulsed Thermal Tomography system upgrade.....	42
4.2. Imaging additively manufactured IN718 nozzle plate	44
4.3. Imaging additively manufactured IN718 particle filter plate	48
5. Conclusions.....	53
References	55

List of Figures

Figure 1 – Principle of pulsed thermal tomography: (a) Schematic drawing (b) Photograph of actual laboratory system.....	9
Figure 2 – Effusivity $e(z)$ for $L=5\text{mm}$ SS316 plate for exact, reconstruction of from analytical model, and reconstruction from COMSOL simulations	14
Figure 3 – Exact effusivity for $L=5\text{mm}$ SS316 plate: (a) Surface plot of $e(x,z)$ (b) Pseudo-color image of $e(x,z)$	14
Figure 4 – Reconstructed effusivity from analytical model for $L=5\text{mm}$ SS316: (a) Surface plot of $e(x,z)$ (b) Pseudo-color image of $e(x,z)$	15
Figure 5 – Reconstructed effusivity from COMSOL heat transfer simulations for $L=5\text{mm}$ SS316: (a) Surface plot of $e(x,z)$ (b) Pseudo-color image of $e(x,z)$	15
Figure 6 – View of COMSOL model metallic plate with cylindrical FBH defect in the center: (a) Front (b) Side	16
Figure 7 –Time evolution of heat transfer through metallic plate (bottom) and concurrent appearance of localized “hot spot” on the plate front surface (top).....	17
Figure 8 – (a) Model showing line of surface temperature data collection (b) A Gaussian curve fit to COMSOL data at time $t=0.21\text{s}$	18
Figure 9 – Increase of observed radius on plate surface with time for a 5mm diameter FBH located at 2mm depth	18
Figure 10 – Estimate of best time for defect detection for 5mm diameter, 2mm deep FBH based on temperature contrast on the plate	19
Figure 11 – Reconstructed effusivity for 5mm diameter FBH located at 1mm depth in 5mm thick SS316 plate (a) Surface plot of $e(x,z)$ (b) Pseudo-color image of $e(x,z)$	20
Figure 12 – Reconstructed effusivity for 5mm diameter FBH located at 1mm depth in 10mm thick SS316 plate (a) Surface plot of $e(x,z)$ (b) Pseudo-color image of $e(x,z)$	21
Figure 13 – Reconstructed effusivity for 5mm diameter FBH defect located at 3mm depth in 10mm thick SS316 plate: (a) Surface plot of $e(x,z)$ (b) Pseudo-color image of $e(x,z)$	21
Figure 14 – (a) “Hot spot” formation for 200 μm diameter FBH (b) Surface temperature profile at 0.3s	22
Figure 15 – Reconstructed effusivity for a 200 μm diameter FBH defect located 1mm depth in 5mm thick SS316 plate (a) Surface plot of $e(x,z)$ (b) Pseudo-color image of $e(x,z)$	23
Figure 16 – Reconstructed effusivity for spherical defect with 3mm diameter (a) Surface plot of $e(x,z)$ (b) Pseudo-color image of $e(x,z)$	24
Figure 17 – Reconstructed effusivity for spherical defect with 1mm diameter (a) Surface plot of $e(x,z)$ (b) Pseudo-color image of $e(x,z)$	24
Figure 18 – Reconstructed effusivity for spherical defect with 200 μm diameter (a) Surface plot of $e(x,z)$ (b) Pseudo-color image of $e(x,z)$	25
Figure 19 – 3-D rendering of FBH pattern in SS316 and IN718 metallic plates	26
Figure 20 – Design of FBH of different diameters and depths relative to plate surface.....	27

Figure 21 – Photograph of FBH pattern in SS316 plate	27
Figure 22 – Imaging of FBH from flat side of the plate: (left) Front view (right) Rear view	28
Figure 23 – Reconstruction of larger FBH in SS316 plate. (Left) Imaged area. (Right) Reconstructed parallel plane slices at 2mm, 3mm, 4mm and 5mm depths.....	29
Figure 24 – Reconstruction of larger FBH cross-sections in SS316 plate. (Left) Parallel plane slice at 4mm depth with vertical lines drawn through same-depth different size FBH (Right) Corresponding cross-section plane slices.....	30
Figure 25 – Reconstruction of smaller FBH in SS316 plate. (Left) imaged area (Right) reconstructed parallel plane slices at 1mm, 2mm, 3mm and 4mm depths	31
Figure 26 – Reconstruction of smaller FBH in SS316 plate. (Left) Parallel plane slice at 3mm depth with vertical lines drawn through same-depth different size FBH (Right) Corresponding cross-section plane slices.....	31
Figure 27 – Reconstruction of larger FBH in NI718 plate. (Left) Imaged area. (Right) Reconstructed parallel plane slices at 3.2mm, 4.2mm, 5.2mm and 6.2mm depths	32
Figure 28 – Reconstruction of larger FBH cross-sections in NI718 plate. (Left) Parallel plane slice at 5.2mm depth with vertical lines drawn through same-depth different size FBH (Right) Corresponding cross-section plane slices.....	33
Figure 29 – Reconstruction of smaller FBH in NI718 plate. (Left) Imaged area. (Right) Reconstructed parallel plane slices at 2.2mm, 3.2mm, 4.2mm and 5.2mm depths	34
Figure 30 – Reconstruction of smaller FBH cross-sections in NI718 plate. (Left) Parallel plane slice at 3.2mm depth with vertical lines drawn through same-depth different size FBH (Right) Corresponding cross-section plane slices.....	35
Figure 31 – Design of FBH of different diameters and depths relative to plate surface in SS304, Ni200, and C276 plates	36
Figure 32 – Photograph of FBH pattern in C276 plate	36
Figure 33 – Reconstruction of smaller depth FBH in SS304 plate. (Left) Imaged area. (Right) Reconstructed parallel plane slices at 1mm, 2mm, and 3mm depths.	37
Figure 34 – Reconstruction of larger depth FBH in SS304 plate. (Left) Imaged area. (Right) Reconstructed parallel plane slices at 4mm, 5mm, and 6mm depths	38
Figure 35 – Reconstruction of smaller depth FBH in NI200 plate. (Left) Imaged area. (Right) Reconstructed parallel plane slices at 1.3mm, 2mm, and 3mm depths.....	39
Figure 36 – Reconstruction of larger depth FBH in NI200 plate. (Left) Imaged area. (Right) Reconstructed parallel plane slices at 4mm, 5mm, and 6mm depths	39
Figure 37 – Reconstruction of smaller depth FBH in C276 plate. (Left) Imaged area (Right) Reconstructed parallel plane slices at 1mm, 2mm, and 3mm depths	40
Figure 38 – Reconstruction of larger depth FBH in C276 plate. (Left) Imaged area (Right) Reconstructed parallel plane slices at 4mm, 5mm, and 6mm depths	41
Figure 39 – Screenshot of GUI for converting output of Research IR software to match file requirements of effusivity reconstruction code	43

Figure 40 – Photograph of PTT setup imaging of IN718 nozzle plate with new FLIR X8500sc imaging camera	44
Figure 41 – (a) Photograph of the IN718 nozzle plate (b) Highlighted area imaged with PTT....	44
Figure 42 – Reconstruction of parallel slices of IN718 nozzle plate at 0.67mm, 1mm, 1.2mm, and 1.35mm depths.....	45
Figure 43 – Reconstruction of 3-D effusivity of IN718 nozzle plate (Left) Parallel slice at 1.35mm depth (Right) Vertical cross-section slices	46
Figure 44 – Screen capture of 3-D imaging of Inconel 718 nozzle plate with ImageJ software package.....	47
Figure 45 – 3-D imaging of NI718 nozzle plate reconstructions with MATLAB	48
Figure 46 – Photograph of PTT laboratory setup for imaging of IN718 particle filter plate with new FLIR X8500sc imaging camera.....	49
Figure 47 – Photograph of the filter plate (a) top view (b) bottom/side view	49
Figure 48 – Reconstruction of parallel slices of IN718 particle filter plate top face at estimated 1mm, 1.35mm, 1.65mm, and 1.9mm depths	50
Figure 49 – Reconstruction of 3-D effusivity of IN718 filter plate (Left) Parallel slice at 1.9mm depth (Right) Vertical cross-section slices	51
Figure 50 – Reconstruction of parallel slices of IN718 particle filter plate side face at estimated 0.75mm, 0.9mm, 1.1mm, and 1.3mm depths	52

List of Tables

Table 5 – Estimated detection limits for cylindrical FBH defects in SS316.....	22
Table 2 – Parameters of X8500sc camera	42

Abstract

Additive manufacturing (AM, or 3D printing) for commercial nuclear energy applications is an emerging method for cost-efficient manufacturing aimed at replacing aging nuclear reactor parts and reducing costs for new construction. Because of the geometry of metallic structures of interest for nuclear applications, which consist of planar primitives with no symmetry of revolution, limited options are available for nondestructive evaluation (NDE), either during or post manufacturing. Known material flaws in AM include low-density regions consisting of non-sintered powder, which have to be detected to ensure the safety of long-term performance nuclear reactor components. As a solution to NDE of AM, we are developing pulsed thermal tomography (PTT) models and depth inversion algorithms for 3D imaging. PTT has many advantages because the method is non-contact and allows for in-service, NDE of AM nuclear reactor parts. By analyzing transients of surface temperature response due to internal thermal resistances, one can obtain 3D reconstructions of material effusivity using a unique inversion algorithm developed at Argonne.

This report provides results of preliminary performance evaluation of PTT capability in detection of flaws in metallic structures, as well imaging complex geometry AM structures. Performance of PTT was investigated through modeling and experiments, Computer models of PTT were developed using COMSOL Heat Transfer module. Defects were modeled as cylindrical flat bottom holes (FBH), which is a common model of calibrated material flaws in thermal tomography experiments. Materials considered in this study include stainless steel 316 (SS316), stainless steel 304 (SS304), and Inconel 718. Theoretical analyses were conducted to validate inversion of simulated PTT data with COMSOL for a plate. Subsequently, 3D reconstructions were performed on COMSOL simulations for FBH, revealing a decrease in spatial resolution over depth due to thermal diffusion. The results of this study show that the performance of the inversion algorithm for detecting smaller defects depends strongly on the depth of the defect as well as the incident heat flux. The size of detectable defect was estimated by fitting a Gaussian function to surface temperature profile. The criteria for detectability was taken as 20mK noise equivalent temperature difference (NETD), which is currently the sensitivity limit of high-performance infrared cameras. It was determined through computer simulations that the smallest detectable FBH in SS316 has a 50 μ m diameter and is located 0.5mm below the plate surface.

Preliminary experimental studies were performed to evaluate PTT performance in detecting calibrated flaws using metallic specimens with AM defects simulated as drilled-in FBH's. High strength Stainless Steel 316 and Inconel 718 alloys were considered, as well as lower grade Stainless Steel 304, Nickel 200, and Hastelloy C276. Specimens investigated in this report consisted of approximately 1/4in-thick plates made out of these alloys using conventional manufacturing methods. The diameters of FBH's varied from 1mm to 8mm, and their depths below the plate flat surface varied between 1mm and 6mm. The size of the smallest FBH was limited to 1mm because conventional mechanical drills were used for creating the holes. PTT imaging results have shown that 1mm-diameter FBH located 1mm and 2mm below the surface were detectable. Larger size FBH were detectable at greater depth. For example, 6mm-diameter FBH could be

detected at 8mm depth. Image contrast varied slightly between the specimens, with the best reconstructions obtained in SS316 and C276 plates.

Finally, PTT capability in imaging several AM structures fabricated from Inconel 718 (IN718) powder feedstock was investigated. The AM structures have complex geometry, but do not have calibrated internal defects. The objective is to determine PTT settings, such as the total integration time, for imaging of representative AM structures. A new FLIR X8500sc IR camera with higher spatial resolution (1280x1024 at 181Hz frame rate) was integrated into the PTT laboratory setup. Software tools were developed to ensure compatibility of new camera files with legacy effusivity reconstruction codes. The new camera was used to obtain 3-D reconstructions of AM IN718 nozzle plate and a particle filter plate. It was shown that PTT can scan through 2/3in-thick Inconel 718 plates in approximately 15s. Several modes of 3-D data visualization were explored, including using ImageJ and MATLAB software packages. The results demonstrate the capability of PTT in 3-D imaging of complex geometry AM structures. Intermediate results demonstrated in this report will be developed further to investigate detection of flaws in AM specimens.

1. Introduction

1.1. Background

Additive manufacturing (AM) for nuclear energy applications is an emerging method for cost-efficient manufacturing aimed at replacing aging nuclear reactor parts and reducing costs for new construction of advanced reactors [1,2]. However, there are still challenges for widespread deployment of AM in nuclear reactors, particular the ability to perform nondestructive evaluation (NDE) of AM parts. Because of the intrinsic features of AM process for fabricating stainless steel and nickel super alloys metallic parts, such as direct laser sintering (DLS), defects can appear consisting of low density regions or pores. Porosity can be introduced into AM parts due to incomplete melting of the powder particles or insufficient overlapping of the melt pools [3]. Oscillations in the surface of the melt pool caused by rapid heating and cooling result in powder ejection and splattering of the melt, resulting in surface roughness and porosity [4]. Furthermore, improper cooling rates can cause the formation of non-equilibrium phases and residual stresses, requiring post-process heat treatments [5-7]. The pore is potentially a seed for crack formation in the structure due to non-uniform expansion of the material in response to thermal and mechanical stresses in nuclear reactor [8,9]. Pores have been observed in destructive examinations to be on the order of 20 μ m and larger.

Currently, there exist limited options for nondestructive examination (NDE) of AM structures either during or post-manufacturing. During manufacturing phase, spatial constraints of the 3-D printer limit deployment of many conventional NDE systems, such as radiography. Furthermore, in DLS manufacturing, a metallic part is covered by un-sintered powder. This prevents the use of contact methods, such as ultrasound, and obscures signals from non-contact methods, such as passive thermography. In post-manufacturing phase, complex shapes composed of planar geometrical primitives with lack of rotational symmetry make it difficult to perform digital radiography. Contact NDE techniques, such ultrasound, would be difficult because AM structures have rough surfaces which affects probe coupling. In addition, NDE methods such as ultrasound and eddy currents require time-consuming point-by-point raster scanning of specimens. As a solution to NDE of AM structures, Argonne is developing pulsed thermal tomography (PTT) models and depth inversion algorithms for 3D imaging and flaw detection. PTT obtains reconstruction of material internal defects by monitoring surface temperature transients following thermal pulse applied to material surface. The method is non-contact, with measurements performed from stand-off distance from one side of the specimen. An imaging camera with megapixel array of detector elements acquires an image of a large section of material. This allows for detection of flaws with minimal amount of mechanical scanning.

A schematic depiction of the PTT setup is shown in Figure 1(a), with the photograph of the laboratory system presented in Figure 1(b). The method consists of illuminating material with white light flash lamp, which rapidly deposits heat on the material surface [10,11]. Heat transfer then takes place from the heated surface to the interior of the sample, resulting in a continuous decrease of the surface temperature. A megapixel fast frame infrared (IR) camera records time-resolved images of surface temperature distribution $T(x,y,t)$. The acquired thermal-imaging data

therefore consist of a series of 2D images of the sample's surface temperature at consecutive time instants. The unique reconstruction algorithm of PTT developed at Argonne obtains thermal effusivity $e(x,y,z)$ from time-dependent surface temperature $T(x,y,t)$ measurements.

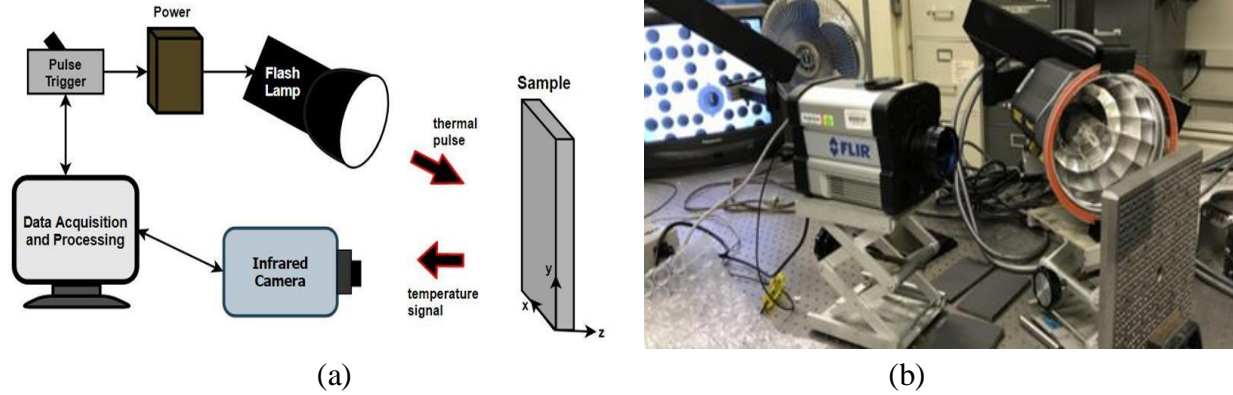


Figure 1 – Principle of pulsed thermal tomography: (a) Schematic drawing (b) Photograph of actual laboratory system

1.2. Overview

Project objectives addressed in this report include development of performance metrics for PTT detection of flaw size and flaw location relative to material surface. Section 2 describes analytical and computational modeling efforts. We used COMSOL computer simulations with the Heat Transfer module to investigate the performance of the PTT method. Materials modeled in COMSOL computer simulations included high strength corrosion-resistant stainless steel (SS) 316 and 304, and Inconel 718 alloys, which are commonly used materials for liquid sodium and light water cooled reactors, respectively. We represented defects as cylindrical flat bottom holes (FBH) with varying sizes and located at various depths. FBH is a common model of calibrated material defects in thermal tomography experiments [11]. In computer simulations, surface temperature transient data $T(x,y,t)$ was calculated with COMSOL, and reconstruction of 3D material effusivity $e(x,y,z)$ was performed with an inversion algorithm developed at Argonne and implemented in MATLAB [12]. Transverse size of defects was estimated from surface temperatures by fitting a Gaussian curve and applying detection threshold equal to noise equivalent temperature difference (NETD) of existing state-of-the-art IR cameras. Based on simulation results, we conclude that the inversion algorithm is more suitable for depth detection, while transverse size (radius) of the defect can be efficiently obtained from surface temperature. Effectiveness of 3D reconstruction depended greatly on the depth of the defect as well as incident heat flux, which affects temperature contrast in the image. Further studies using spherical defects were also performed to model more realistic defects observed in AM parts.

Section 3 described preliminary experimental results of PTT performance evaluation using calibrated defects in high-strength metallic alloys commonly used as reactor structural materials [13]. These include stainless steel 316 and Inconel 718 alloys, as well as lower grade stainless steel 304, nickel 200, and hastelloy C265. Calibrated flaws consisted of cylindrical FBH's of variable

diameter and depth drilled in metallic plates. The results obtained thus far indicate that PTT can image flaws 1mm in size, which is the smallest calibrated flaw created in metallic specimens. Consistent with computer modeling in Section 2, results of experiments in Section 3 indicate the general trend in PTT performance that smaller defects can be detected when they are closer to the surface

Finally, in Section 4 we describe the preliminary results of evaluating the capability of PTT system in imaging of complex geometry AM metallic specimens [14]. These specimens do not have calibrated internal defects. The objective of imaging is to determine PTT settings, such as the total integration time, to image several representative AM structures. The laboratory PTT system was upgraded with a new FLIR X8500sc imaging camera with higher spatial resolution and sensitivity. Using the new camera, 2/3in thick IN718 nozzle plate and a section of a filter plate manufactured with direct laser sintering (DLS) method were imaged. Reconstructions demonstrate that PTT is capable of imaging through all specimens in approximately 15s. Conclusions and brief future work are outlined in Section 5.

2. Modeling of Pulsed Thermal Tomography Performance

2.1. Mathematical basis of Pulsed Thermal Tomography

The reconstruction algorithm of pulsed thermal tomography (PTT) obtains thermal effusivity $e(z)$ as a function of depth (z) from time-dependent surface temperature $T(t)$ measurements or that from simulation data [12]. Under ideal thermal tomography conditions, the theoretical model for the algorithm is based on the solution to the 1D heat conduction equation. Heat propagation through the metallic plate is approximately one-dimensional for an instantaneous, uniform pulse of thermal energy.

The algorithm starts with the assumption that the medium can be treated as semi-infinite, with corrections developed during reconstruction. For semi-infinite slabs, heat diffusion can be modeled with 1D equation

$$\frac{\partial T}{\partial t} = \alpha \frac{\partial^2 T}{\partial z^2} \quad (1)$$

where z is the depth coordinate, x and y are coordinates in the transverse plane, and α is thermal diffusivity defined as

$$\alpha = k/\rho c \quad (2)$$

Here, k is thermal conductivity, ρ is density, and c is specific heat. The analytic solution is given as [11, 15,16]

$$T(z,t) = \frac{Q}{\sqrt{\rho c k \pi t}} e^{-\frac{z^2}{4\alpha t}}, \quad 0 \leq z \leq \infty \quad (3)$$

where Q is the instantaneously deposited surface thermal energy density (J/m^2), and e is the thermal effusivity, which is a measure of how the material exchanges thermal energy with its surroundings given as

$$e = \sqrt{\rho c k} \quad (4)$$

This allows one to express observed or apparent time-dependent effusivity of the medium as

$$e(t) = \frac{Q}{T(z=0,t)\sqrt{\pi t}} \quad (5)$$

One can calculate the maximum of thermal wavefront velocity $\partial T/\partial z$ by setting

$$\frac{\partial^2 T}{\partial z^2} = 0 \quad (6)$$

which gives characteristic relationship between time and depth

$$z = \sqrt{\pi \alpha t} \quad (7)$$

The next crucial step is to recognize that $e(z)$ and $e(t)$ can be related through a convolution integral, where $1/z$ is the transfer function [10]

$$e(t) = \int_0^z z^{-1} e(\zeta) d\zeta \quad (8)$$

Taking z -derivatives of both sides,

$$e(z) = \frac{d}{dz} (ze(t)) = \frac{d}{dz} \left(\frac{zQ}{T(t)\sqrt{\pi t}} \right) \quad (9)$$

one can simplify the equation by using Eqn. (7) to obtain

$$e(z) = \frac{d}{dz} \left(\frac{\sqrt{\alpha} Q}{T(t)} \right) \quad (10)$$

To calculate the derivate, one has to relate dz to dt using Eqn. (7)

$$dz = \frac{\sqrt{\pi \alpha}}{2\sqrt{t}} dt = \frac{\sqrt{\pi \alpha}}{2} \frac{\sqrt{\pi \alpha}}{z} dt = \frac{\pi \alpha}{2z} dt \quad (11)$$

Therefore, the z -derivative of a function f can be written as

$$\frac{df}{dz} = \frac{df}{dt} \frac{dt}{dz} = \frac{2z}{\pi \alpha} \frac{df}{dt} \quad (12)$$

such that the final equation is

$$e(z) = z \frac{2Q}{\pi \sqrt{\alpha}} \frac{d}{dt} \left(\frac{1}{T(t)} \right) \Bigg|_{t=z^2/\pi \alpha} \quad (13)$$

so that spatial reconstruction of effusivity is given as a product of depth function z and time derivative of the inverse of surface temperature evaluated at time t corresponding to depth z according to Equation (7).

2.2. Validation of Effusivity reconstruction with COMSOL simulated data

Before analyzing detection of small defects with COMSOL, fidelity of COMSOL simulated data was evaluated by performing of reconstruction for a structure for which there exists a closed form analytical solution. An example chosen in this study is a plate with infinite transverse dimensions and finite thickness L , for which the analytic solution for transient surface temperature as a function of time is given as [10,11]

$$T(z=0,t) = \frac{Q}{\rho c L} \left[1 + 2 \sum_{n=1}^{\infty} \exp\left(-\frac{n^2 \pi^2}{L^2} \alpha t\right) \right] \quad (14)$$

Here $T(t)$ is the change in temperature relative to the value before the thermal impulse Q was applied. Note that the steady-state temperature $T=Q/\rho c L$ is a restatement of the familiar expression $q=mc\Delta T$ for a plate. Generating data for $T(t)$ using Equation (14), one can perform reconstruction procedure using Equation (13). For reference, actual effusivity $e(z)$ given as

$$e(z) = \begin{cases} \sqrt{\rho c k}, & 0 \leq z \leq L \\ 0, & z > L \end{cases} \quad (15)$$

Validations of COMSOL data inversion involved modeling heat diffusion in a 5cmx5cmx0.5cm SS316 plate. Diffusion of heat in a plate with such geometry (transverse dimensions are 10x larger than the thickness) closely resembles the case of an infinite plate of finite thickness. Using the inversion algorithm, thermal effusivity using COMSOL surface temperature data and the analytic solution for temperature decay were compared. For direct comparison with the analytical model, thermophysical properties of SS316 in the COMSOL model were kept constant.

Figure 2 shows reconstructions of $e(z)$ for $L=5\text{mm}$ SS316 plate with $\rho=7954 \text{ kg/m}^3$, $k=13.96 \text{ W/m}^2\text{K}$, $c = 499.07 \text{ J/kg}$. The graphs are plotted for exact effusivity given by Equation 15, effusivity reconstructed from the analytical model of Equation 14, and effusivity reconstructed from COMSOL simulation data. Figure 3 shows exact effusivity $e(x,z)$ plotted as 3D surface and 2D pseudo-color image. Figure 4 shows effusivity reconstructed from the analytical model plotted as 3D surface and 2D pseudo-color image. Figure 5 shows effusivity $e(x,z)$ reconstructed from COMSOL heat transfer simulations, which is plotted as 3D surface and 2D pseudo-color image. Note that reconstruction of effusivity either from the analytical model or from COMSOL simulations is an approximation which smooths out the sharp edge in the back of the metallic plate. Effusivity reconstruction from COMSOL simulations have a delayed rise at the front surface of the plate, and contain ripples. We attribute that to simulated data artifacts, particularly the temperature sampling rate. Temperature data for COMSOL simulations in Figures 2 and 5 was sampled at 0.005s intervals. We observed that quality of reconstruction was lower for lower sampling frequency. Sampling at higher rate was challenging because of limited computer

workstation memory (64GB). We conclude that, when the known artifacts in the data are taken into account, COMSOL can be used as a data generation platform for analyzing PTT performance.

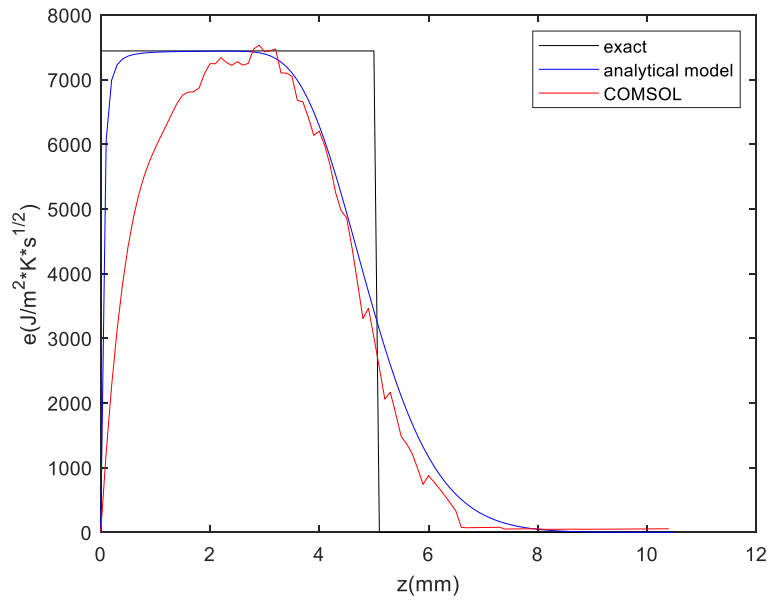


Figure 2 – Effusivity $e(z)$ for $L=5\text{mm}$ SS316 plate for exact, reconstruction of from analytical model, and reconstruction from COMSOL simulations

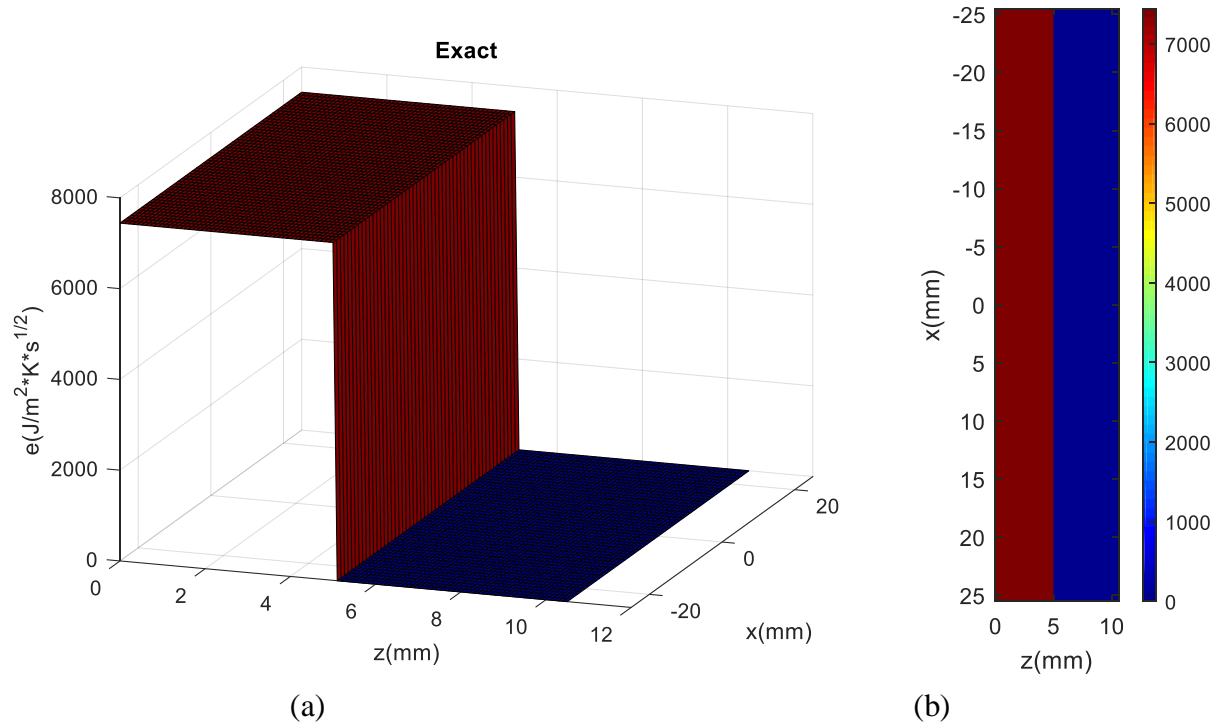


Figure 3 – Exact effusivity for $L=5\text{mm}$ SS316 plate: (a) Surface plot of $e(x,z)$ (b) Pseudo-color image of $e(x,z)$

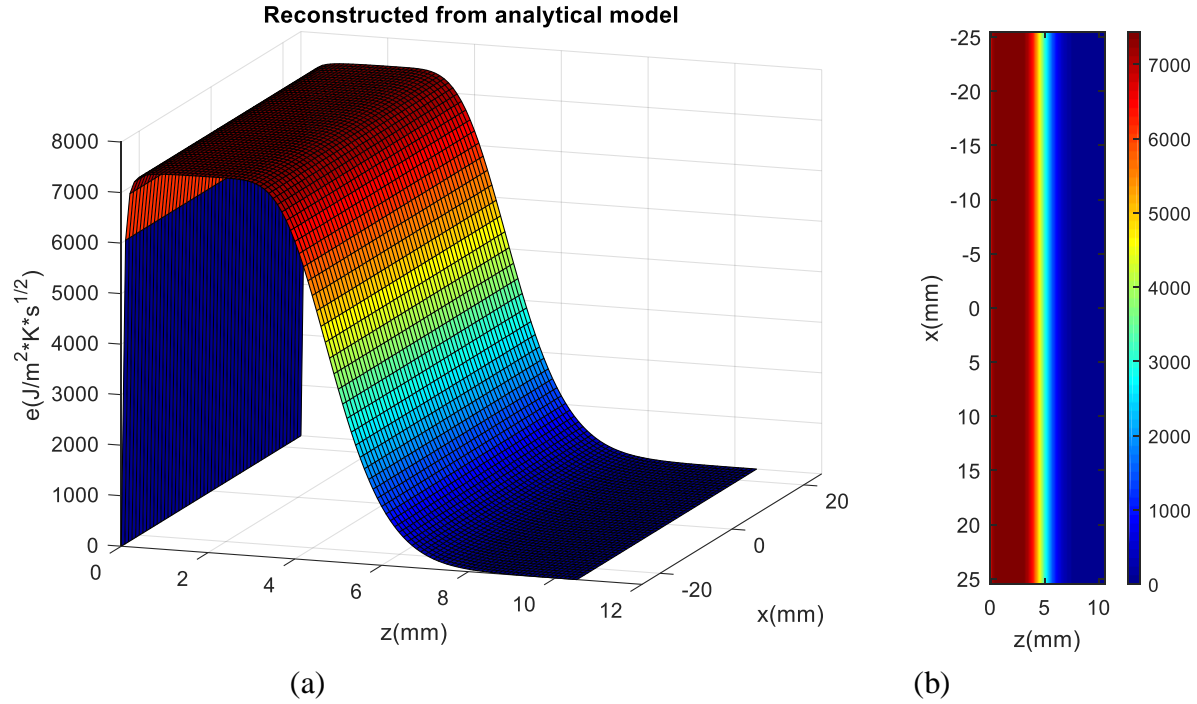


Figure 4 – Reconstructed effusivity from analytical model for L=5mm SS316: (a) Surface plot of $e(x,z)$ (b) Pseudo-color image of $e(x,z)$

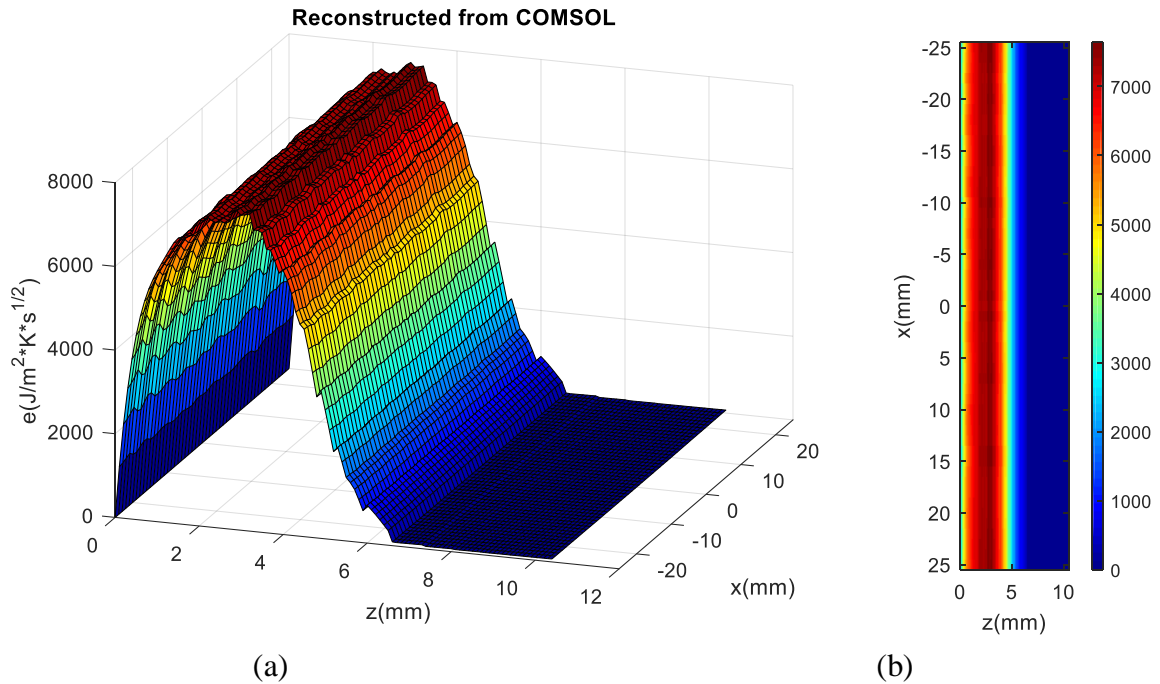


Figure 5 – Reconstructed effusivity from COMSOL heat transfer simulations for L=5mm SS316: (a) Surface plot of $e(x,z)$ (b) Pseudo-color image of $e(x,z)$

2.3. Modeling of Internal Defect Detection

2.3.1. Basic Principles of Internal Flaw Detection with Thermal Tomography

Internal material flaws, which are localized regions of lower density compared to the host matrix, can be detected with thermal tomography by observing surface temperature transients. The basic principle that flaw with lower density provides thermal resistance to diffusing heat flux. This causes appearance of temperature gradient on the material surface due to spatial variation of temperature decay. In particular, temperature “hot spots” can be observed on the material surface above the flaw. To visualize flaw detection, COMSOL simulations were performed for a structure consisting a 5cmx5cmx1cm metallic plate with cylindrical flat bottom hole (FBH) defects. An example of a structure used in simulations, consisting of a stainless steel plate with a 5mm diameter, 3mm deep FBH defect is shown in Figure 6. An FBH is a common model of material flaw used in thermal tomography calibration studies. The FBH defect was filled with air to approximately model the un-sintered powder in AM defects which has a lower density and hence lower thermal conductivity than that of the metallic plate

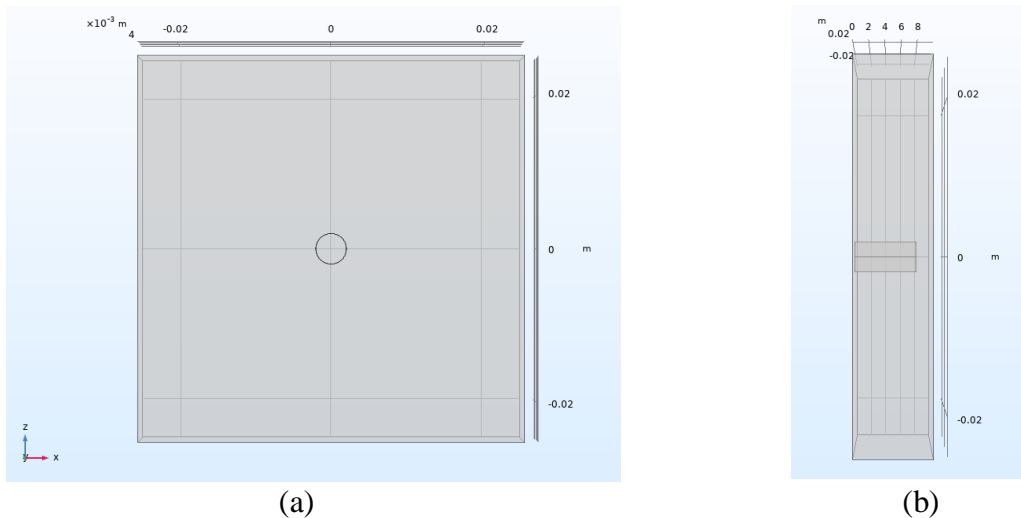


Figure 6 – View of COMSOL model metallic plate with cylindrical FBH defect in the center: (a) Front (b) Side

Appearance of the “hot spot” can be observed in the sequence of frames shown in Figure 7, which displays time evolution of heat transfer through a metallic plate with an FBH defect. Pseudo-color map with warm colors (red, yellow) corresponding to higher temperatures and cold colors (green, blue) corresponding to lower temperatures is used for display temperature distribution. A uniform thermal pulse of energy incident from the right propagates through the material until encountering an internal defect. Thermal diffusion in the region above the defect is therefore reduced as a result of this metal to air discontinuity which creates a “hot spot,” seen on the front surface of the plate. The radius of the FBH is directly related to the radius of the “hot spot.” The latter increases in size over time due to diffusion of heat around the surface of the FBH in the radial

direction. A procedure for finding the best threshold criteria to measure the radius of the FBH defect from surface temperature observations is discussed in the next section.

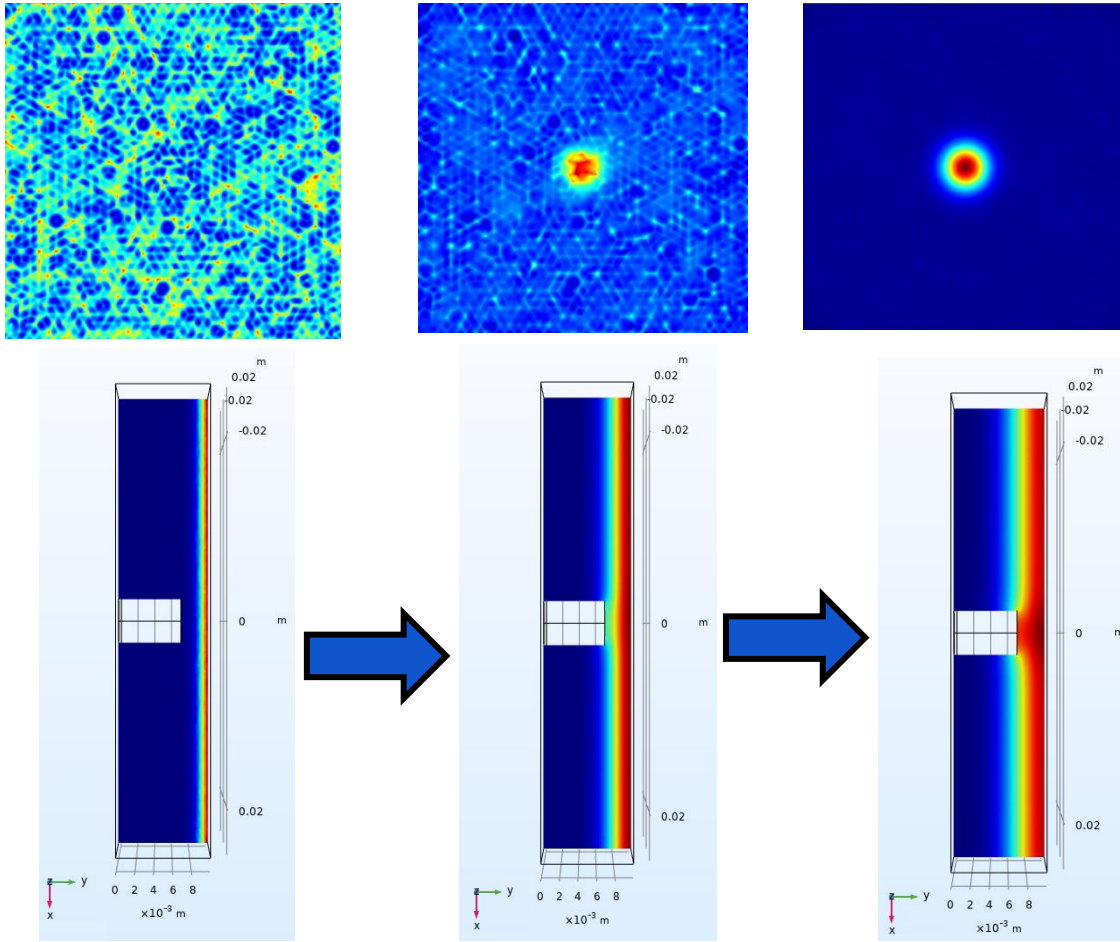


Figure 7 –Time evolution of heat transfer through metallic plate (bottom) and concurrent appearance of localized “hot spot” on the plate front surface (top)

2.3.2. Estimation of internal defect transverse size from COMSOL simulations

A procedure for estimating transverse size of internal defects based on observations of surface temperature transients was developed and evaluated using COMSOL simulations. Estimation of flaw size in simulations was accomplished by collecting 1D temperature data across a center line on the front surface of the plate, as shown in Figure 8. We determined radial temperature distribution of the surface “hot spot” is Gaussian, which is expected since the governing process is diffusion. Therefore, we defined the radius of the “hot spot” to be the distance from the center of the spot where temperature has the maximum value to the point where the temperature decreases by a factor of $1/e$. For a Gaussian distribution with standard deviation σ , the radius at $1/e$ of the maximum temperature would be represented by $\sqrt{2}\sigma$. An example of Gaussian curve fitting is shown below in Figure 8 for the case of a 5mm diameter FBH defect located at 2mm depth below the surface of the plate. Temperature along the line drawn on the surface of the 5cmx5cmx1cm

plate in Figure 8(a) at time $t=0.21\text{s}$ after heat pulse application is plotted in Figure 8(b). A Gaussian fit is shown to closely agree with the temperature data.

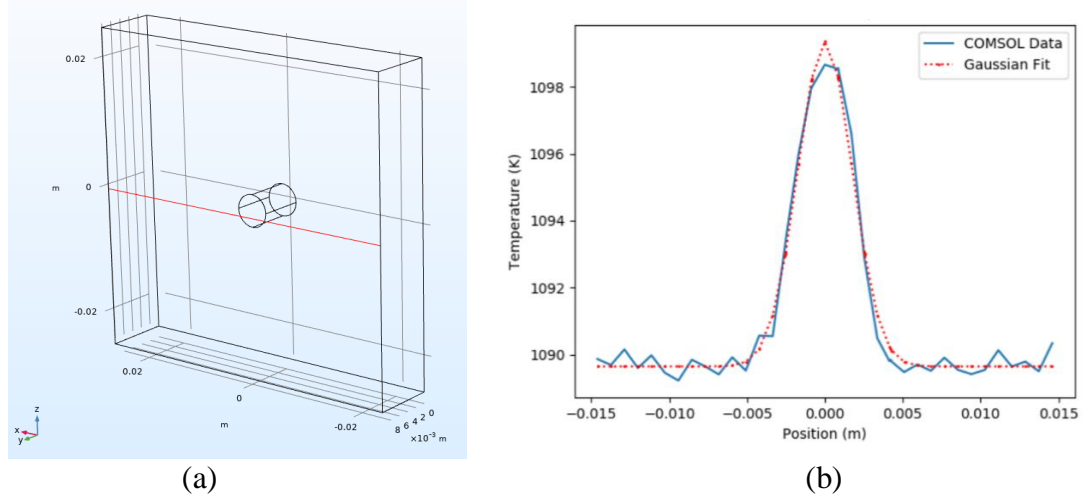


Figure 8 – (a) Model showing line of surface temperature data collection (b) A Gaussian curve fit to COMSOL data at time $t=0.21\text{s}$

We observed that the “hot spot” radius increases with time, which we attribute to heat diffusion around the FBH cylindrical surface. An example of this phenomena is displayed in Figure 9 for the plate in Figure 8 with 5mm diameter FBH located at 2mm depth. The radius of the “hot spot” almost doubles in 2s. Thus, one has to define a time to measure the “hot spot” to obtain the most accurate estimate of the FBH size. This earliest observation time was chosen based on the sensitivity of the IR camera used in experiment. This study focuses on high-end cameras (e.g. FLIR X8501sc) with noise equivalent temperature difference (NETD) of 20mK to find the limit to defect detection. For more compact but less sensitive cameras (e.g. FLIR A65sc) with NETD of 50mk, the criteria for radial detection will be slightly different.

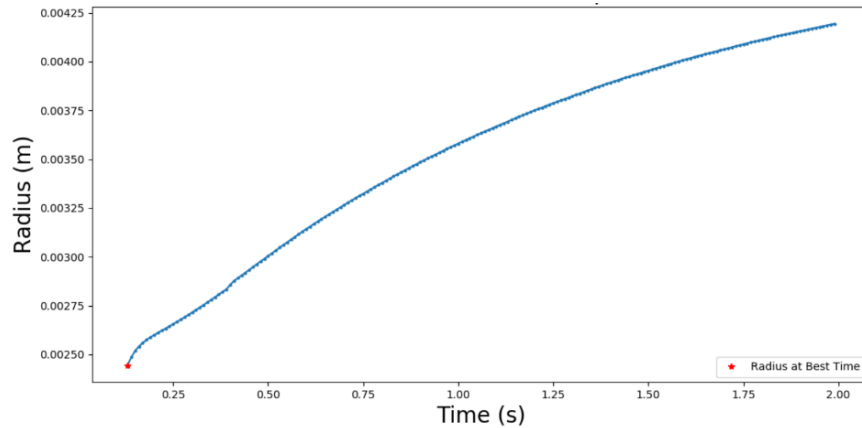


Figure 9 – Increase of observed radius on plate surface with time for a 5mm diameter FBH located at 2mm depth

By selecting the time at which the “hot spot” temperature begins to exceed 20mK relative to the average plate temperature, one could determine the best time for FBH radius estimation. This time represented the start of “hot spot” appearance on the surface, at which point the radius of the “hot spot” provides the best approximation to the internal defect radius.

To further elucidate the validity of this criteria, Figure 10 shows the divergence of temperature decay curves at a region directly above the defect, and near the edge of the plate (several centimeters away from the defect). The time at which the two curves begin to diverge for the first time corresponds to the time at which the “hot spot” first begins to appear on the plate surface.

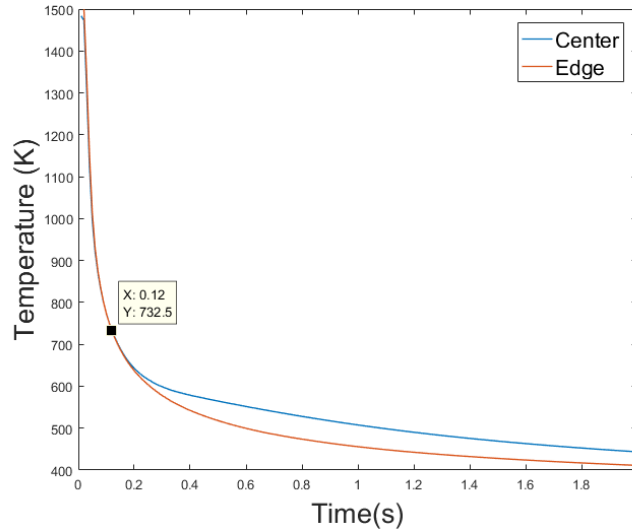


Figure 10 – Estimate of best time for defect detection for 5mm diameter, 2mm deep FBH based on temperature contrast on the plate

It is important to note that radial estimates of internal defects closer to the surface of the metallic plate are more accurate than those for defects located deeper within the plate. Given enough time for the heat to traverse the plate, the “hot spots” eventually appear on the surface of the plate regardless of how deep the defect is. However, accuracy of transverse size and depth location of the flaw estimates progressively decreases due to the effects of thermal diffusion. During the initial period, heat diffusion is predominantly in 1D. However, with increasing time and depth within the plate, heat diffuses in lateral directions as well, which leads to blurring of the “hot spot” and decrease in the accuracy of radius and depth estimation of the FBH.

2.3.4. Defect reconstruction from COMSOL simulations

As described in Section 2.1, effusivity reconstruction algorithm uses time-dependent surface temperature data to create an image of defect within the metallic plate. Following validation study described in Section 2.2, inversion algorithm was applied to COMSOL simulations data for a SS316 metallic plate with 5cmx5cm cross-section containing an internal FBH defect. Reconstructions performed for 5mm diameter FBH located 1mm depth in 5mm and 10mm thick SS316 plates are shown in Figures 11 and 12, respectively. Reconstruction of effusivity for 5mm diameter FBH located 3mm depth in 10mm thick SS316 plate is shown in Figure 13. All figures

shows 3D surface plots and pseudo-color images of $e(x,z)$. In all figures, thermal pulse is incident from the left. Warmer red colors signify the heat propagation through the plate and colder blue tones show the front and end boundaries of the metallic plate.

The images of reconstructed effusivity show that the depth of the defect is correctly determined from the inversion algorithm. The first minima in the effusivity plots represent the approximate location of the top of the FBH defect. Effusivity drops to near zero once the heat propagates to the surface of the high thermal resistance barrier. The effusivity then increases due to the effects of heat diffusion occurring around the cylindrical surface of the FBH. After reaching a maximum, the effusivity decreases once again to represent heat propagation at the end of the metallic plate.

There is noticeable spread in the shape of the cylindrical FBH further within the plate caused by increased radial heat diffusion around the defect with higher thermal resistance. Thus, size detection using the inversion algorithm is more difficult at larger depths when the imaging resolution begins to degrade. At the same time, the inversion algorithm provides a good estimate of the depth of the FBH.

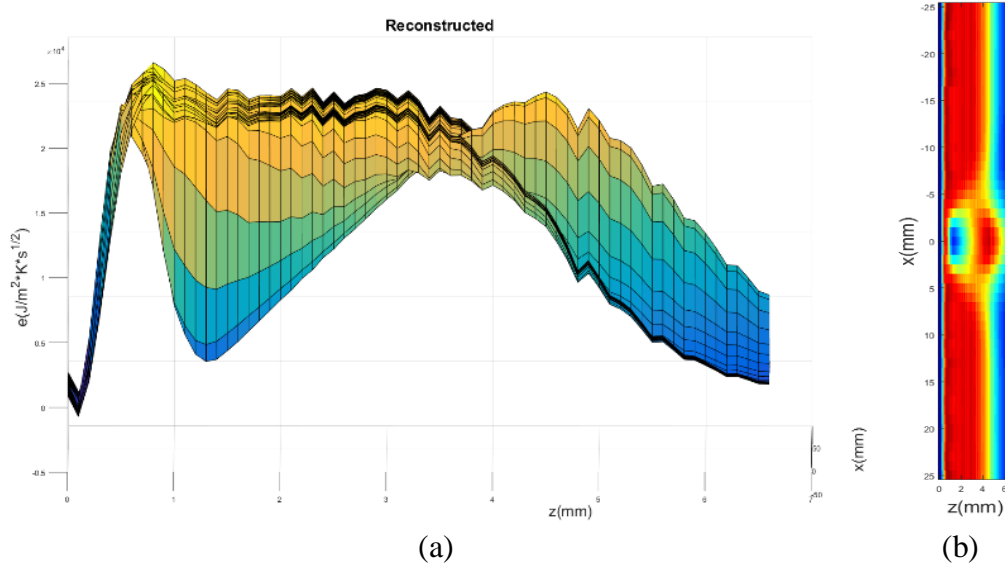


Figure 11 – Reconstructed effusivity for 5mm diameter FBH located at 1mm depth in 5mm thick SS316 plate (a) Surface plot of $e(x,z)$ (b) Pseudo-color image of $e(x,z)$

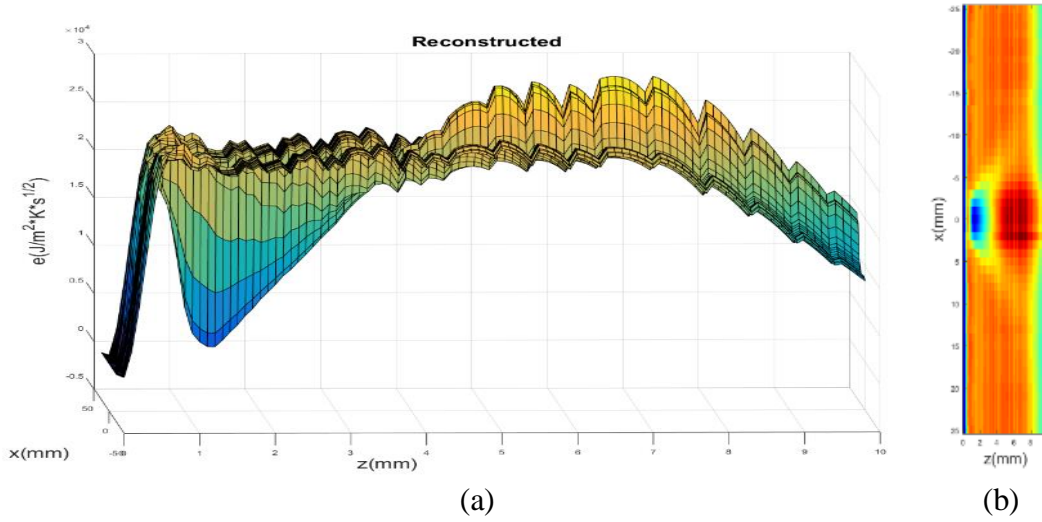


Figure 12 – Reconstructed effusivity for 5mm diameter FBH located at 1mm depth in 10mm thick SS316 plate (a) Surface plot of $e(x,z)$ (b) Pseudo-color image of $e(x,z)$

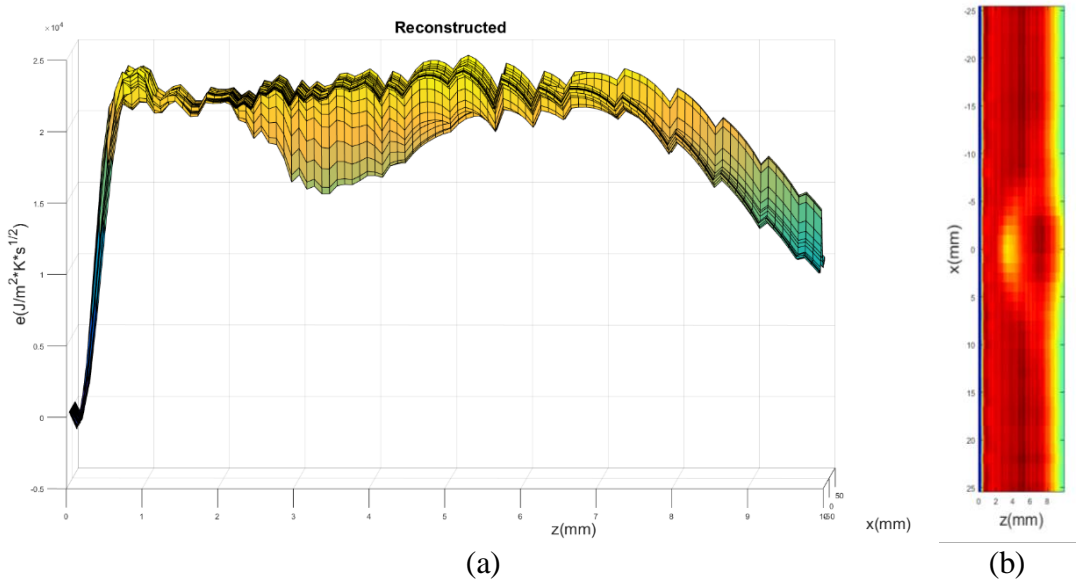


Figure 13 – Reconstructed effusivity for 5mm diameter FBH defect located at 3mm depth in 10mm thick SS316 plate: (a) Surface plot of $e(x,z)$ (b) Pseudo-color image of $e(x,z)$

2.3.5. Estimated limits of defect size detection from COMSOL simulations

PTT performance limits on internal defect size detection were analyzed by using both effusivity reconstruction and “hot spot” size estimation methods using the 20mK temperature difference threshold. COMSOL computer simulations were performed for 5cmx5cmx0.5cm SS316 plates with internal cylindrical FBH defects. An example detection and estimation of effective size of a 200 μ m diameter from the “hot spot” appearing on the surface of the metallic plate is shown in Figure 14. As discussed in Section 3.2, the size of the defect is estimated from the standard deviation σ by fitting a Gaussian curve to the temperature profile.

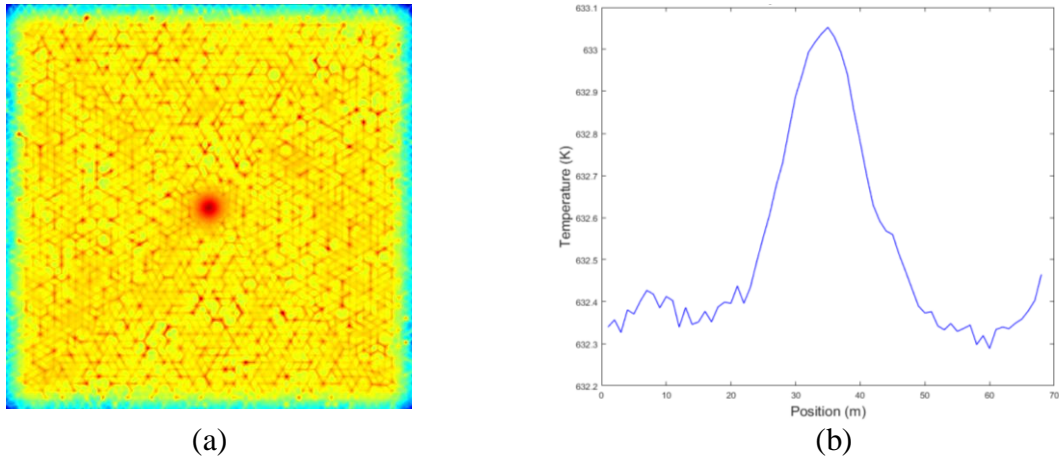


Figure 14 – (a) “Hot spot” formation for 200 μ m diameter FBH (b) Surface temperature profile at 0.3s

Table 5 lists the results for smallest detected diameter of an FBH with corresponding maximum depth of the defect. In general, smaller defects are detectable when they are located closer to the surface. The smallest detectable defect is 50 μ m diameter, which can be detected at the maximum depth of 0.5mm.

Table 1 – Estimated detection limits for cylindrical FBH defects in SS316

Diameter (μ m)	Depth (mm)	Smallest Temp. Difference (mK)
50	0.5	40
70	1	23
200	3	20
700	5	33

Reconstructions of effusivity were also performed to evaluate the capability of inversion algorithm in imaging the smallest defects. Based on results of computer simulations, reconstructions at depths greater than 3mm, have relatively low signal to noise ratio (S/N). Reconstructions with higher S/N would require a larger heat flux (e.g. 10x) than what is currently delivered by the flash lamp in the PTT experimental setup shown in Figure 1. Reconstructed effusivity for a 5mm thick SS316 plate containing a 200 μ m FBH at 1mm depth is shown in Figure 15. The incident heat is

amplified by a factor of 10 relative to COMSOL simulations in previous figures to achieve better imaging contrast. The figure shows 3D surface plot and pseudo-color image of reconstructed $e(x,z)$.

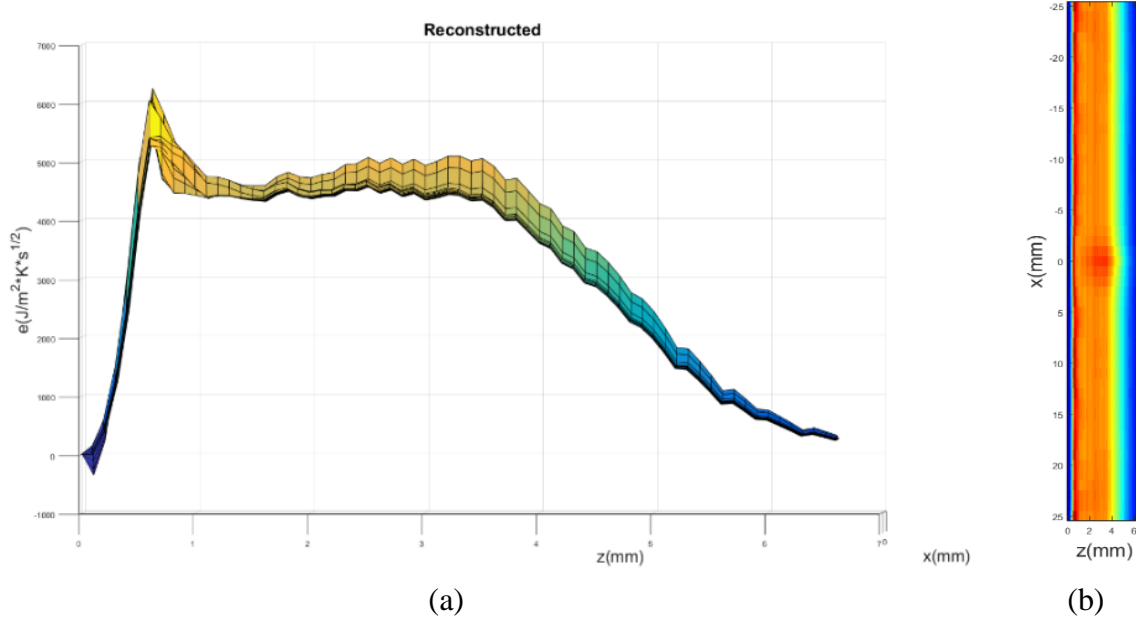


Figure 15 – Reconstructed effusivity for a 200 μm diameter FBH defect located 1mm depth in 5mm thick SS316 plate (a) Surface plot of $e(x,z)$ (b) Pseudo-color image of $e(x,z)$

While FBH is a common model of material flaw in thermal tomography, more realistic model of a defect observed in powder laser sintering-based AM of metals is that of a sphere. Preliminary COMSOL simulations were conducted to model detection of spherical defects in metallic plates. Reconstructions of effusivity were performed for 5cmx5cmx0.5cm SS316 plate containing hollow spheres with diameters of 3mm, 1mm and 200 μm , all located at 1mm depth as measured from the plate surface to the top of respective sphere. Reconstructed effusivity for plates containing 3mm, 1mm and 200 μm diameter spheres is shown in Figures 16, 17 and 18, respectively. Each figure displays surface plot and pseudo-color image of $e(x,z)$. To achieve better contrast in reconstructed image, heat flux was increased by factors of 3 and 10. As seen from reconstructed effusivity plot, the depths of the spheres are accurately measured. Future work will examine detection of spherical-shaped defects in greater detail.

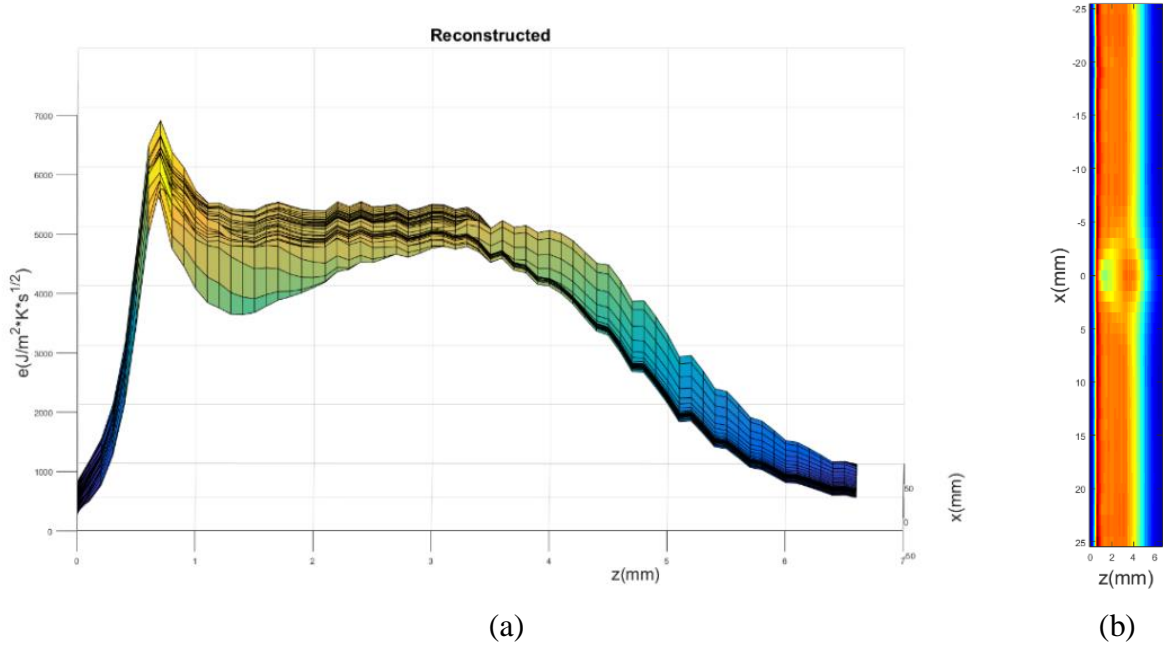


Figure 16 – Reconstructed effusivity for spherical defect with 3mm diameter (a) Surface plot of $e(x,z)$ (b) Pseudo-color image of $e(x,z)$

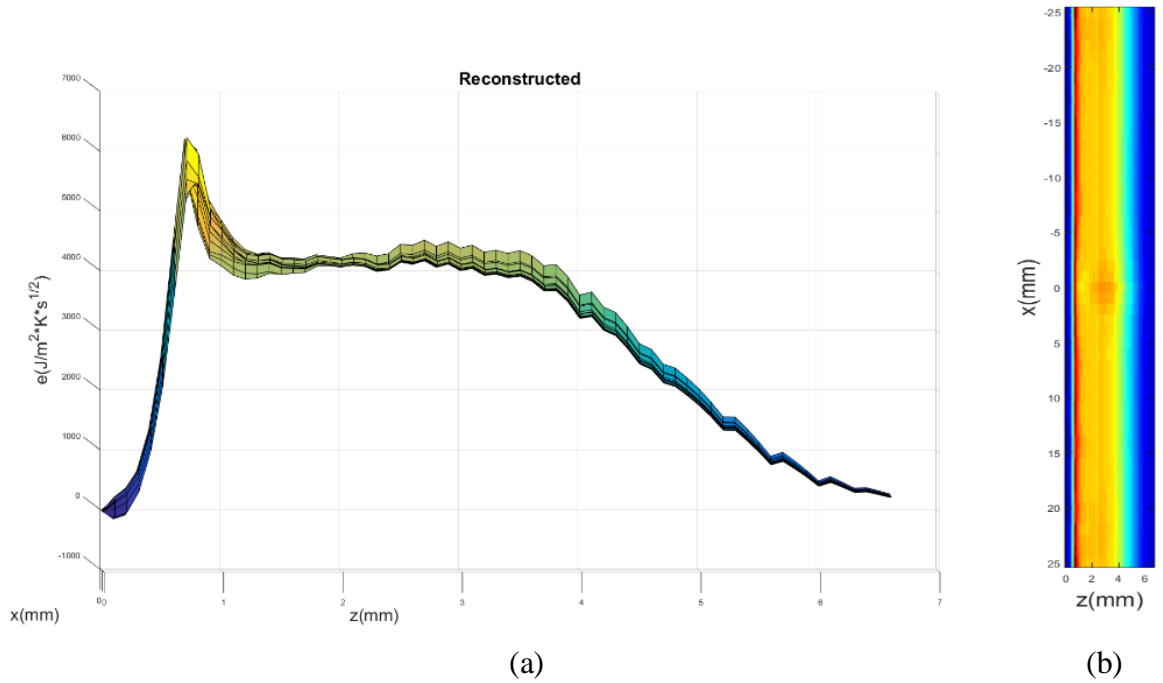


Figure 17 – Reconstructed effusivity for spherical defect with 1mm diameter (a) Surface plot of $e(x,z)$ (b) Pseudo-color image of $e(x,z)$

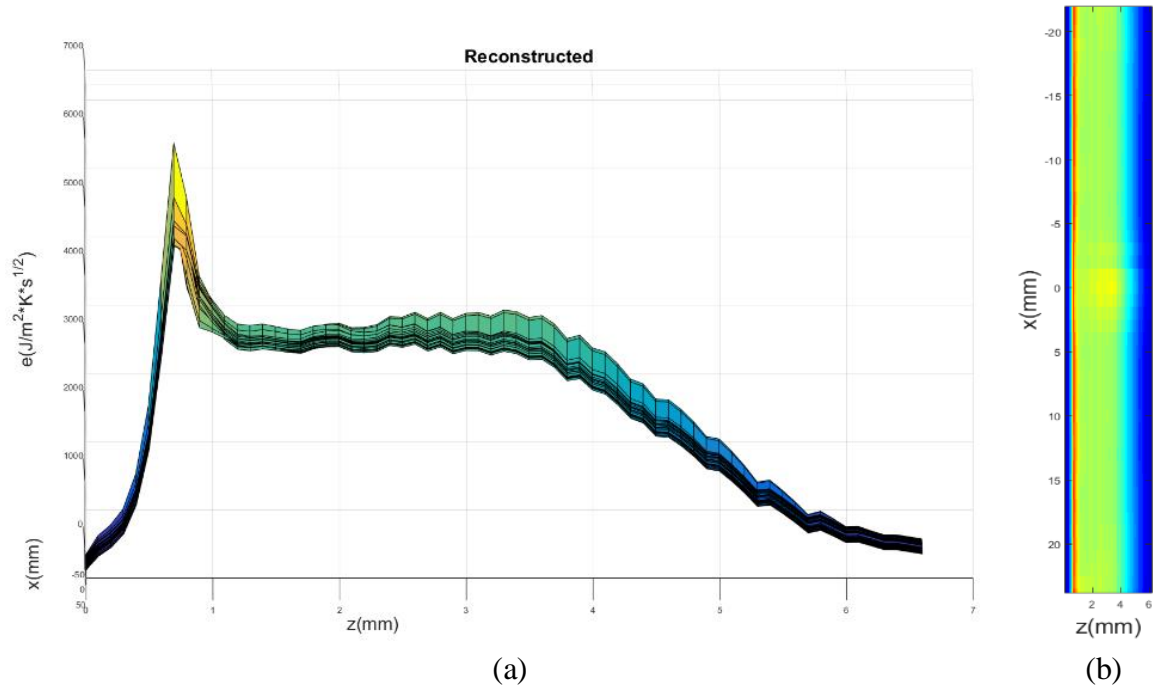


Figure 18 – Reconstructed effusivity for spherical defect with 200 μm diameter (a) Surface plot of $e(x,z)$ (b) Pseudo-color image of $e(x,z)$

3. Imaging of Calibrated Defects in Metallic Specimens

3.1. PTT imaging of calibrated defects in high grade alloys

3.1.1. Development of flat bottom holes in Stainless Steel 316 and Inconel 718 plates

Calibrated defects developed in this project for evaluation of PTT performance consisted of cylindrical flat bottom holes (FBH) of varying size and depth drilled in metallic plates. Producing FBH is a common approach to develop calibrated damage references for thermal tomography performance evaluation. One pattern of holes was designed for metallic plates made of high-strength stainless steel 316 (SS316) and Inconel 718 (IN718) alloys. A computer rendering of the pattern of holes is shown in Figure 19. Figure 20 provides a drawing with labels showing diameters and depths of the holes. Figure 21 shows the photograph of an SS316 plate with FBH. Note that there are two patterns of holes in the plates. Note that the holes diameter decreases along the lines parallel to the longer side of the plate, while the depth along each line is held constant. Along the lines parallel to the shorter side of the plate, the depth increases, while the diameter is fixed. Note that there are two patterns of FBH's on the plate: one with diameters 5,6 and 8mm and depths 2,3,4, and 5mm, and another one with diameters 1,2,3, and 4mm and depths 1,2,3 and 4mm.

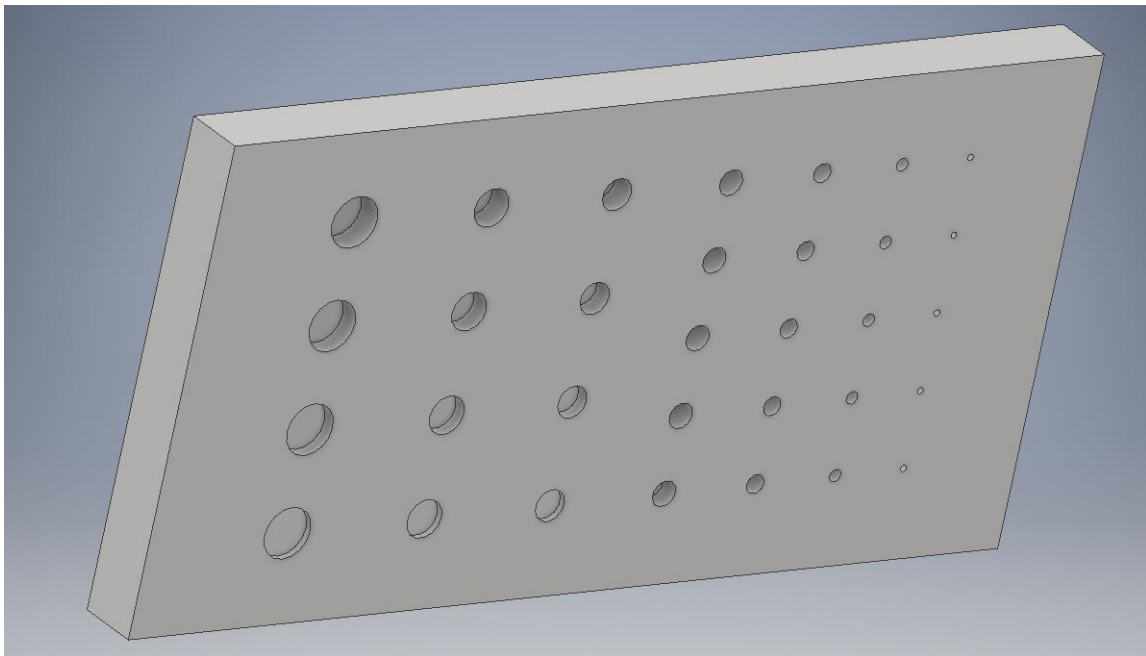


Figure 19 – 3-D rendering of FBH pattern in SS316 and IN718 metallic plates

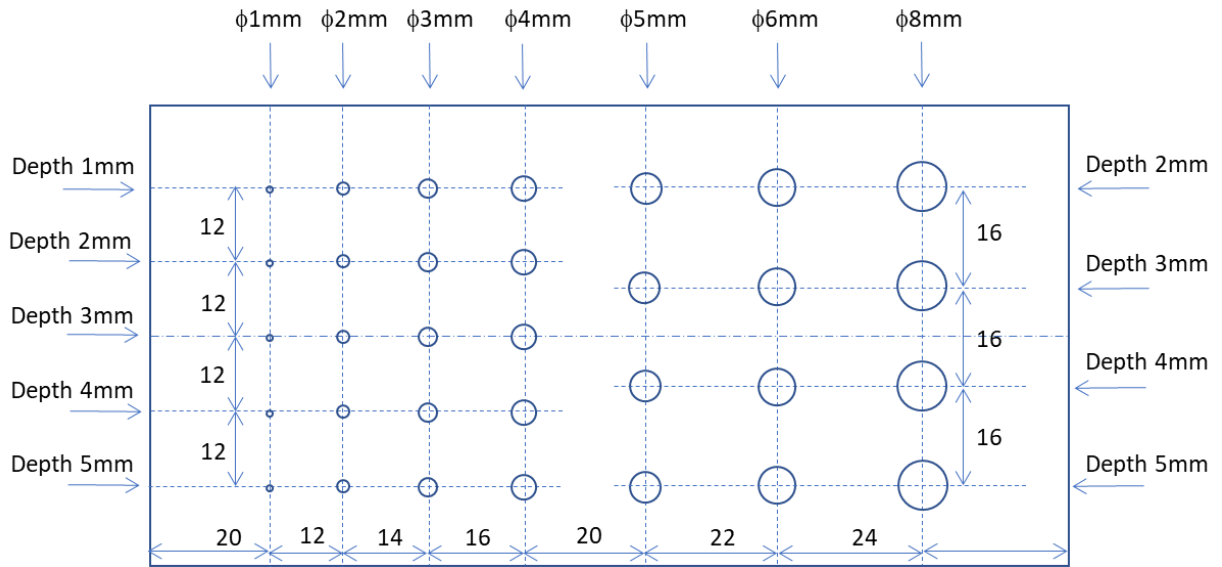


Figure 20 – Design of FBH of different diameters and depths relative to plate surface

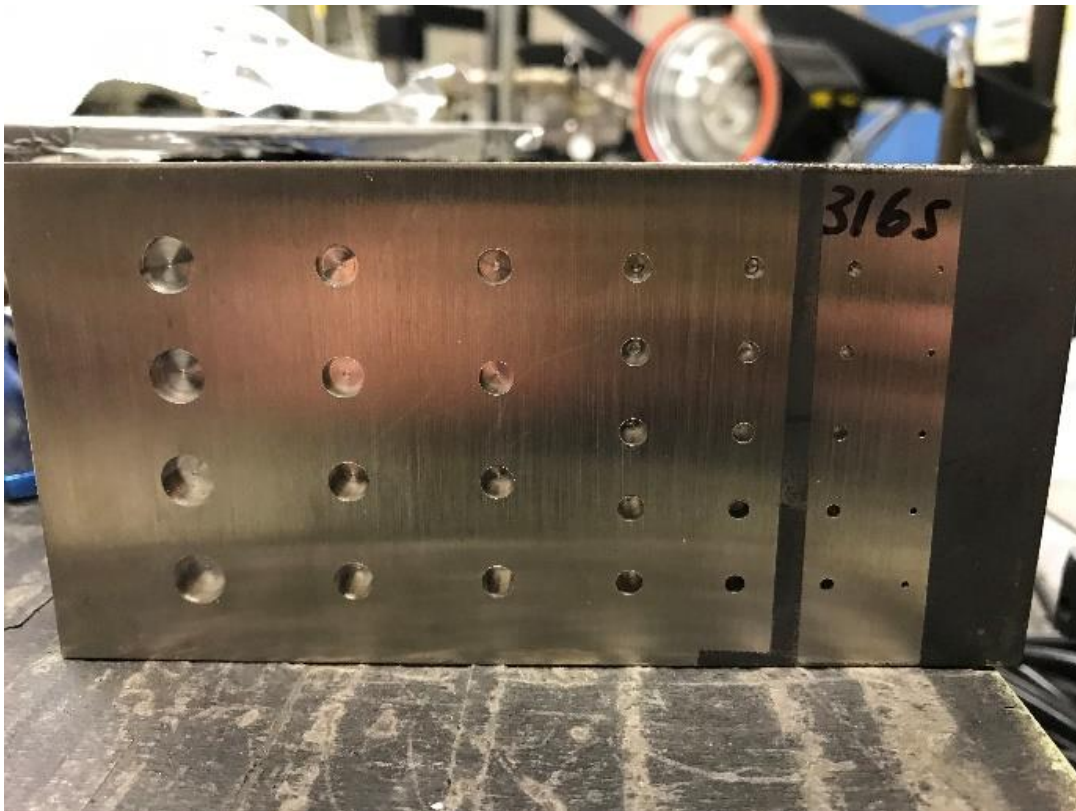


Figure 21 – Photograph of FBH pattern in SS316 plate

The FBH metallic plates were imaged with PTT from the flat side of each plate. Figure 22 shows the photograph of the setup with the flat side of the plate facing the flash lamp and the IR camera.

The back side of plate with visible FBHs is shown in the right panel of Figure 22. For better absorption of thermal energy, all specimens were spray-painted with washable graphite paint. Distribution of incident thermal pulse on the plate is not uniform because the flash light illuminates the metallic plate at an angle. To compensate for this, we have fitted the intensity distribution in the camera frame containing a flash with a polynomial, and then used this polynomial for correction of image intensity in every subsequent frame. The plates were imaged with 320x256 array of pixels at 200Hz resolution rate. The total imaging time to acquire frames for reconstruction of each plate is approximately 10seconds. In the grayscale images, brighter and darker areas indicate higher and lower effusivity, respectively.

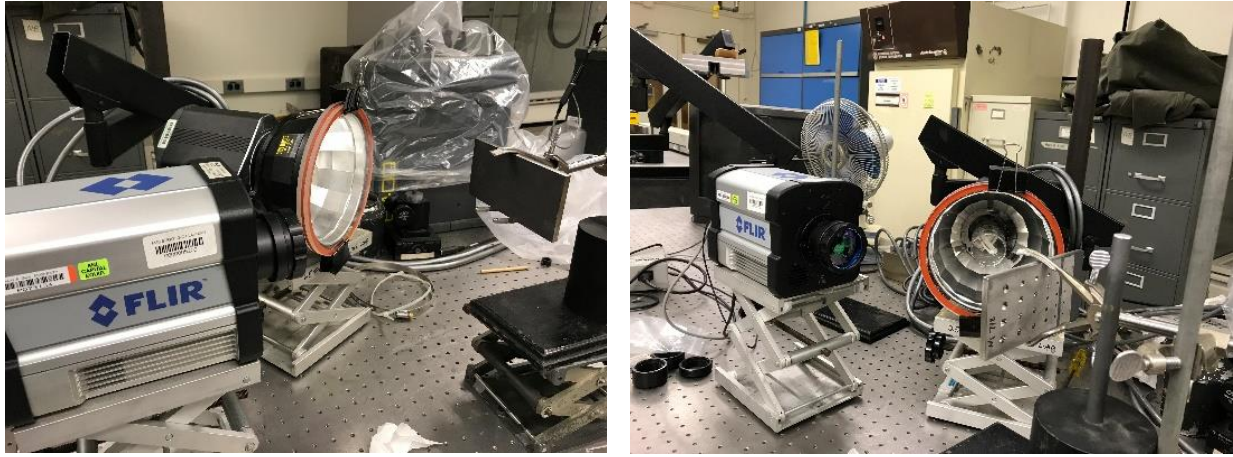


Figure 22 – Imaging of FBH from flat side of the plate: (left) Front view (right) Rear view

3.1.2. PTT imaging of Stainless Steel 316 plate with flat bottom holes

Stainless steel 316 (SS316) is frequently used for manufacturing pressure vessel components in light water and advanced reactors because of the alloys high strength and resistance to corrosion [17]. The SS316 plate with thickness of 6.22mm (0.25in) was produced with conventional metal fabrication techniques. FBH holes in the plate were created by drilling. Because of material high strength, the smallest hole which be created is 1mm diameter. Thermal diffusivity of the SS316 plate was first measured in transmission geometry to determine $\alpha=3.72\text{mm}^2/\text{s}$. This number agrees well with literature value of $\alpha=3.529\text{mm}^2/\text{s}$ [18].

Figure 23 shows reconstructed images of larger FBH at different depths in the material. The left panel of Figure 23 shows the imaged area of the plate. The right panel shows reconstructed parallel plane slices estimated at 2mm, 3mm, 4mm, and 5mm depth. As expected, only the first column of FBH drilled at 2mm depth appear in the parallel place slice at 2mm depth. The column of FBH drilled at 2mm and 3mm depth appear in the plane slice reconstructed at 3mm depth. The pattern continues with three and four columns of FBH appearing in the 4mm and 5mm depth plane slices, respectively. As expected, imaging contrast is better for larger FBH located closer to the surface of the plate. The smallest FBH in the imaged plate area with 5mm diameter can be seen as a faint signature in the 5mm depth reconstruction.

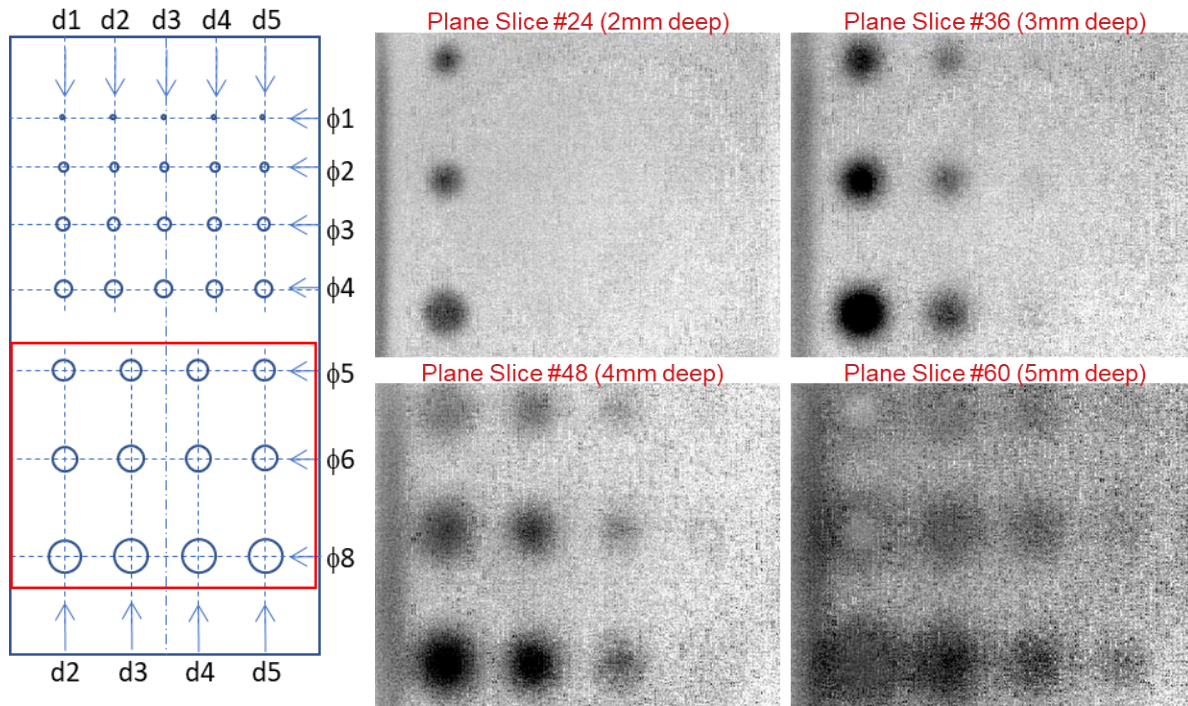


Figure 23 – Reconstruction of larger FBH in SS316 plate. (Left) Imaged area. (Right) Reconstructed parallel plane slices at 2mm, 3mm, 4mm and 5mm depths

Figure 24 shows vertical cross-section reconstructions obtained from the stack of parallel plane slices. The left panel of Figure 11 shows reconstructed parallel plane slice at 4mm depth with vertical lines labeled $i=58$, $i=124$, and $i=195$ (i and j correspond to the indices of individual pixels in the 320×256 imaging matrix of the camera). The vertical lines are drawn through FBH of decreasing size but located at the same depth. Corresponding vertical cross-section reconstructions labeled $i=58$, $i=124$, and $i=195$ with FBH's located at 2mm, 3mm, and 4mm depths, respectively, and are shown in the right panel of Figure 24. Note that the larger diameter hole (8mm) is located on the right side of the each of the vertical reconstruction cross-sections, and the size of the FBH decreases from right to left in the sequence of 8mm, 6mm and 5mm diameters. As expected, reconstruction contrast decreases with decreasing FBH size and increasing depth. Relative sizes of the FBH in the same cross-section slice can be seen to be decreasing right to left. Qualitatively, the FBH in the cross-section slice corresponding to $i=124$ appear to be deeper than the FBH in the cross-section slice corresponding to $i=58$. Similarly, the FBH in the cross-section slice labeled $i=195$ are deeper than those of the cross-section slice corresponding to $i=124$. Because of blurring due to diffusion of the thermal pulse with depth, reconstructed FBH appear as truncated cone shapes.

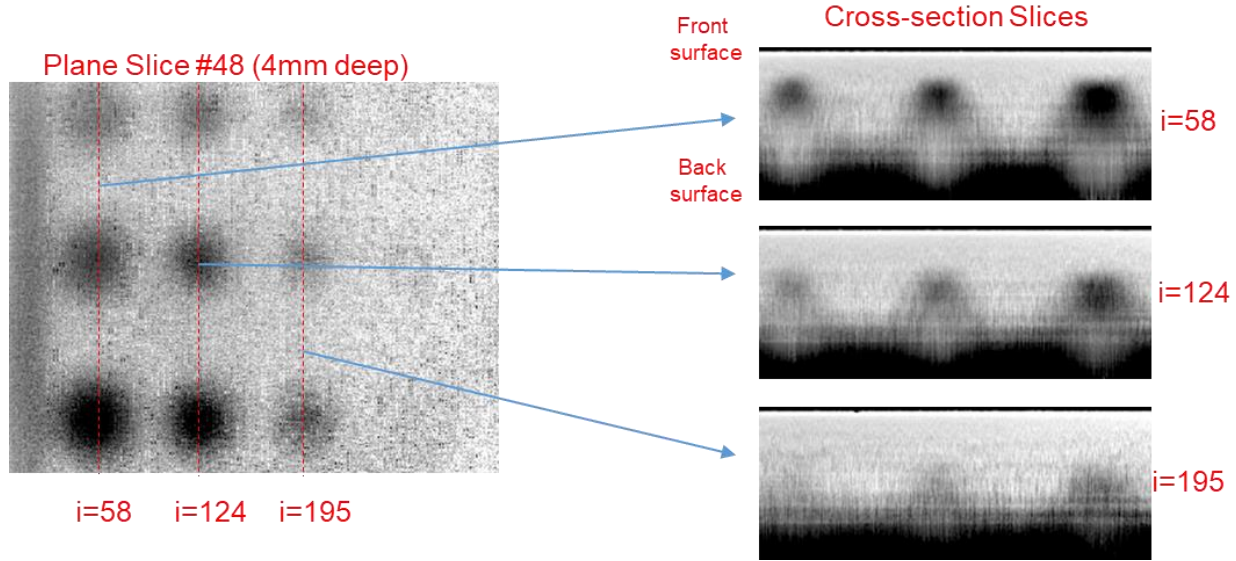


Figure 24 – Reconstruction of larger FBH cross-sections in SS316 plate. (Left) Parallel plane slice at 4mm depth with vertical lines drawn through same-depth different size FBH (Right) Corresponding cross-section plane slices

Figure 25 shows reconstructions of parallel plane slices of smaller FBHs in the SS316 plate. The left panel of Figure 25 indicates the imaging area of the plate. The right panel of Figure 25 contains reconstructions of parallel plane slices at 1mm, 2mm, 3mm and 4mm depths. All FBH down to 1mm size are visible at 1mm depth place slice. At 2mm depth, holes down to 2mm size are clearly visible, and there is a faint signature of the 1mm-diameter FBH. At 3mm depth, the smallest visible FBH is the 2mm-diameter one. At 4mm depth, the 3mm FBH can be detected. Note that these are preliminary qualitative observations. With additional signal processing and thresholding, visibility of smaller size FBH might be enhanced.

Figure 26 shows vertical plane cross-sections reconstructions for the smaller FBH in SS316 plate. The left panel in Figure 26 displays parallel plane cross-section at 3mm depth, with vertical lines $i=58$, $i=108$, and $i=158$ (corresponding to the column labels of the camera 320x256 pixel array), drawn through FBH of different sizes located at the same depth. Corresponding vertical plane cross-section slices are shown in the right panel of Figure 26. As in the case of the larger FBH shown in previous figures, the larger FBH in each cross-section slice is on the right. The FBH's are arranged in a sequence of 4mm, 3mm, 2mm, and 1mm diameters. One can see that in each cross-section slice, the relative size of each cross-section decreases from right to left. The reconstruction of the smallest hole with 1mm diameter can be seen in the cross-section slice corresponding to 1mm depth. At 3mm depth, only the 4mm-diameter hole is visible. As in Figure 24, the shapes of reconstructed FBH's appear as truncated cones.

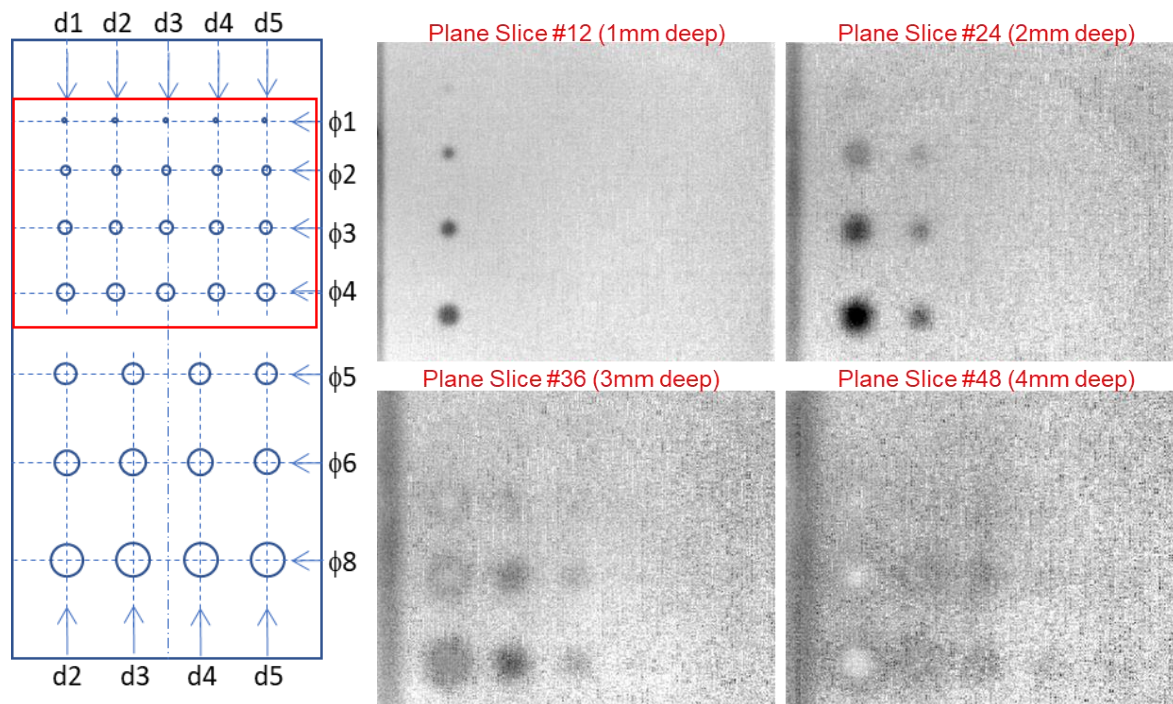


Figure 25 – Reconstruction of smaller FBH in SS316 plate. (Left) imaged area (Right) reconstructed parallel plane slices at 1mm, 2mm, 3mm and 4mm depths

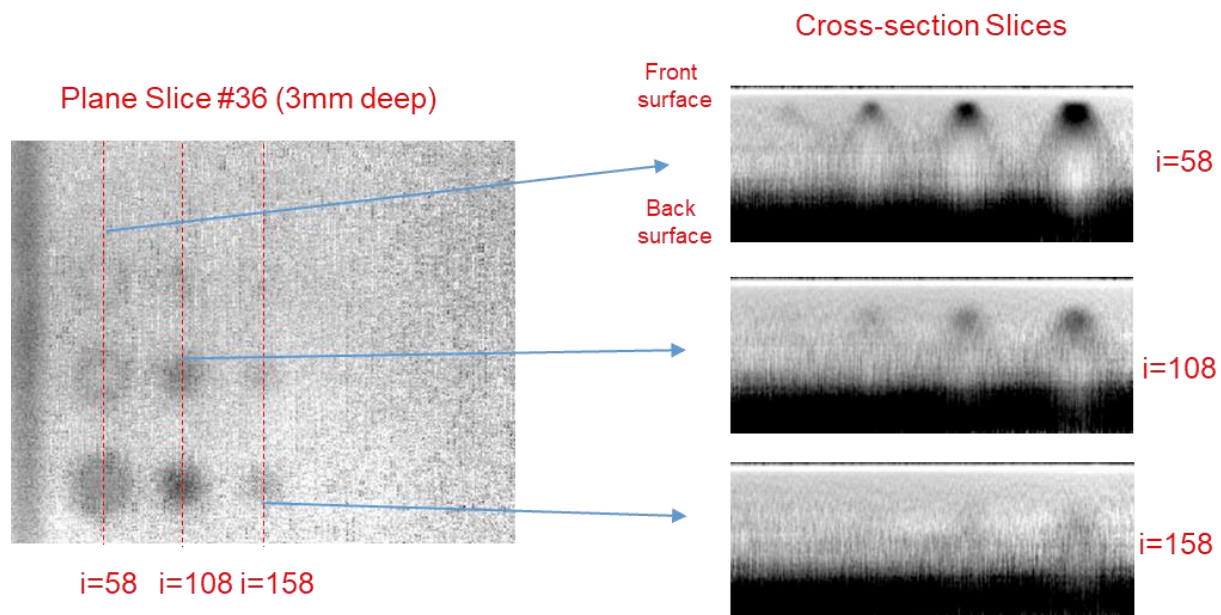


Figure 26 – Reconstruction of smaller FBH in SS316 plate. (Left) Parallel plane slice at 3mm depth with vertical lines drawn through same-depth different size FBH (Right) Corresponding cross-section plane slices

3.1.3. PTT imaging of Inconel 718 plate with flat bottom holes

Inconel 718 (IN718) is used for manufacturing of components inside the pressure vessel as an alternative to SS316. The 7.4mm (0.3in) thick IN718 plate used in this project was produced with conventional metal fabrication techniques. FBH in the plate were created by drilling. Because of the material high strength, the smallest hole which could be drilled out is 1mm diameter. Transmission geometry measurement of was performed to determine thermal diffusivity to be $\alpha=2.82 \text{ mm}^2$ for this plate. Note that thermal diffusivity of IN718 plate is smaller than that of the SS316 plate. Therefore, quality of reconstruction for IN718 specimen is expected to be lower than what was observed for SS316 plate.

Parallel plane slice reconstructions of larger FBH's in the IN718 at various depths are shown in Figure 27. Left panel of Figure 27 shows the imaged area, which consists of larger FBH's in the IN718 plate. The right panel of Figure 27 shows parallel plane slices at 3.2mm, 4.2mm, 5.2mm, and 6.2mm depth. The first three reconstructed images show clearly identifiable FBH's, while the last reconstruction at 6.2mm depth is becoming difficult to interpret. The smallest FBH of 5mm size can be seen in the 5mm depth plane slice.

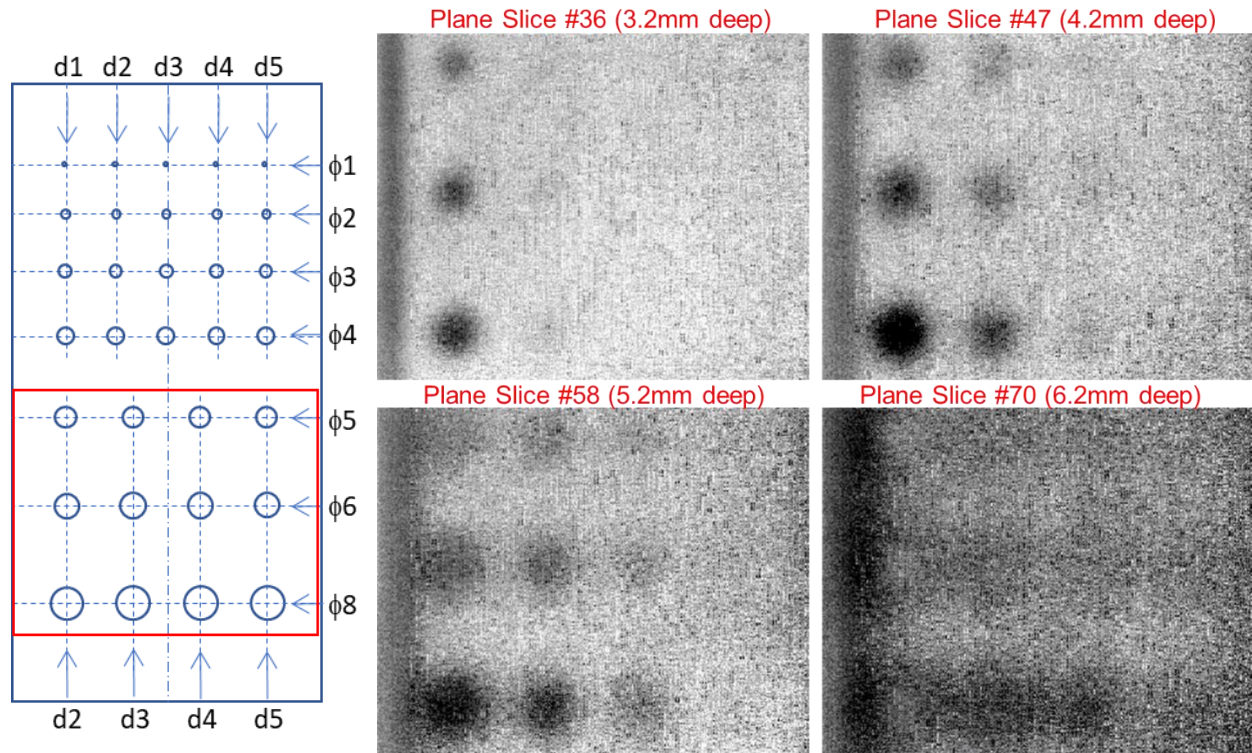


Figure 27 – Reconstruction of larger FBH in IN718 plate. (Left) Imaged area. (Right) Reconstructed parallel plane slices at 3.2mm, 4.2mm, 5.2mm and 6.2mm depths

Reconstructions of cross-section plane slices of larger FBH are shown in Figure 28. The left plane of the figure shows parallel plane slice at 5.2mm depth with vertical lines $i=54$, $i=126$, and $i=194$ (corresponding to pixel column index in the 320x256 array) drawn through FBH of decreasing

size but located at the same depth. The right plane of Figure 28 shows corresponding vertical cross-section slices reconstructions. The cross-section labeled $i=54$ shows reconstructions of FBH of size 8mm, 6mm, and 5mm located at depth 2mm. The cross-sections $i=126$ and $i=194$ shows reconstructions of the same size FBH located at depths 3mm and 4mm, respectively. In each cross-section slice, the size of FBH is decreasing right to left. The smallest 5mm-diameter hole is visible at 3mm depth ($i=126$). At 4mm depth, the 5mm-diameter FBH has very faint signature. Compared to similar size and depth FBH for SS316, the images for IN718 are slightly more blurred. This is to be expected since thermal diffusivity of IN718 is smaller than that of SS316.

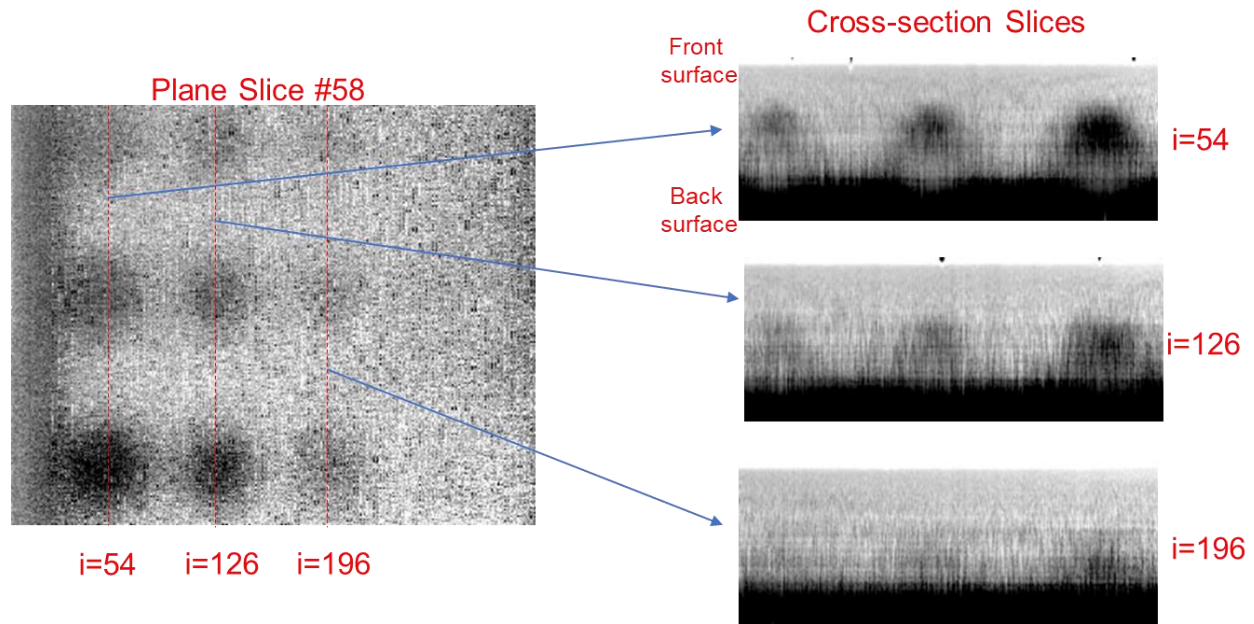


Figure 28 – Reconstruction of larger FBH cross-sections in IN718 plate. (Left) Parallel plane slice at 5.2mm depth with vertical lines drawn through same-depth different size FBH (Right) Corresponding cross-section plane slices

Figure 29 shows reconstructions of smaller FBH in IN718 plate. The left panel shows the imaged area of the plate. The right panel shows the imaged area of the plate. The right panel shows reconstructed parallel plane slices at 2.2mm, 3.2mm, 4.2mm, and 5.2mm depths. The smallest hole with 1mm diameter is faintly visible in the 2.2mm depth plane slice. The plane slice at 3.2mm depth show the first three columns of the FBH. The smallest visible FBH is the one with 2mm diameter. Reconstruction at 4.2mm depth shows blurry images of holes, with the smallest FBH of 3mm diameter. The plane reconstructed at 5.2mm shows faint indications of FBH with 3mm and 4mm diameters.

Figure 17 shows vertical cross-section reconstructions of the smaller FBH in the IN718 plate. Parallel plane slice at 3.2mm depth is shown in the left part of the figure with vertical lines labeled $i=58$ and $i=108$ drawn through the FBH of decreasing size, which are located at the same depth in the plate. As in the prior discussion, i is the index of the pixels column in the 320x256 array. Right

panel of Figure 30 contains corresponding vertical cross-section reconstructions. The images labeled $i=58$ and $i=108$ correspond to FBH's located at 1mm and 2mm depths, respectively. The images show vertical profiles of FBH with diameters 4mm, 3mm, 2mm, and 1mm, with the FBH size decreasing from right to left. Because of blurring with increasing depth, the shapes of FBH cross-sections appear to be dome-shaped. Qualitatively, the images provide enough information to detect decrease in FBH sizes. The smallest FBH which can be observed is the 2mm-diameter hole. As mentioned above, the quality of reconstruction of FBH in IN718 plate is lower than that in the SS316 plate because of lower value of thermal diffusivity on IN718.

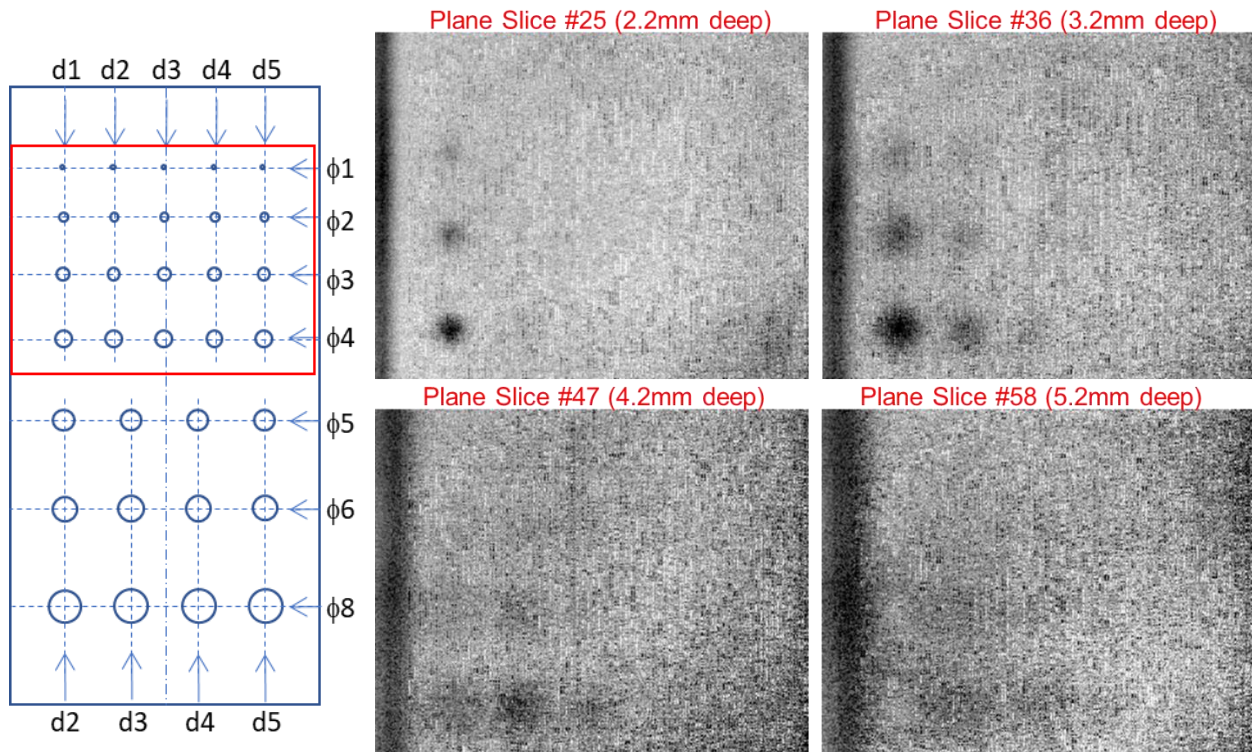


Figure 29 – Reconstruction of smaller FBH in IN718 plate. (Left) Imaged area. (Right) Reconstructed parallel plane slices at 2.2mm, 3.2mm, 4.2mm and 5.2mm depths

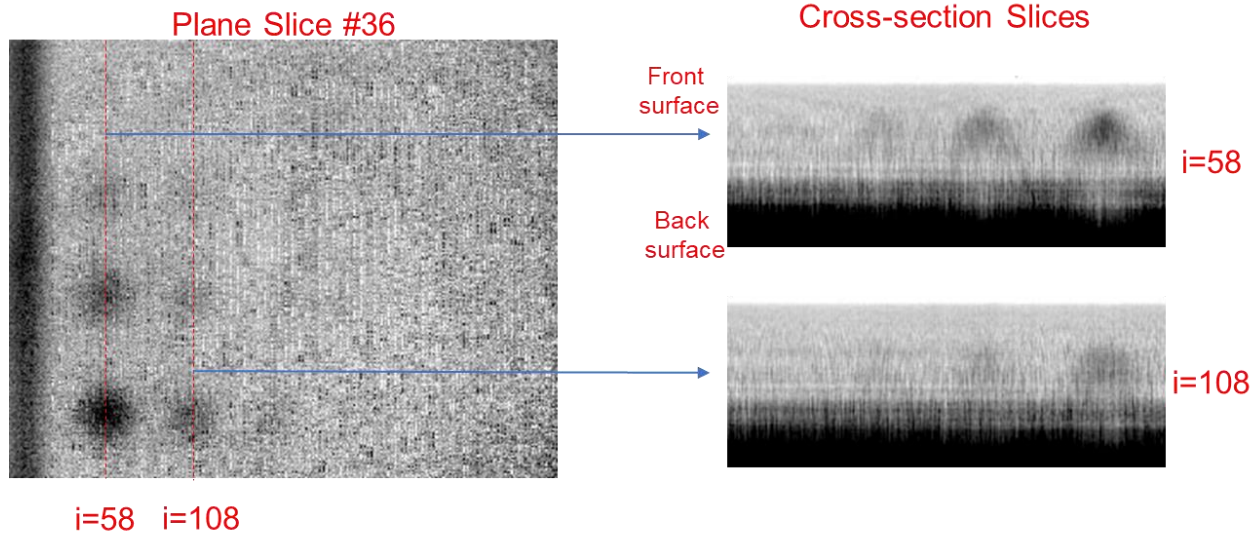


Figure 30 – Reconstruction of smaller FBH cross-sections in NI718 plate. (Left) Parallel plane slice at 3.2mm depth with vertical lines drawn through same-depth different size FBH (Right) Corresponding cross-section plane slices

3.2. PTT imaging of calibrated defects in lower grade alloys

3.2.1. Development of calibrated flat bottom holes Stainless Steel 304, Nickel 200 and Hastelloy C276 specimens

Another set of FBH was designed for metallic plates made out of lower strength grade stainless steel 304 (SS304), Nickel 200 (Ni200), and Hastelloy C276 (C276). The design of pattern of these FBH's is shown in Figure 31. A photograph showing the C276 plate with FBH is displayed in Figure 32. In this pattern, hole diameters are 1,2,4 and 8mm, while depths are 1,2,3,4,5 and 6mm. Along the lines parallel to the longer plate side, FBH diameter is fixed while depth decreases. Along the lines parallel to the shorter plate side, FBH depth is constant while the diameter decreases.

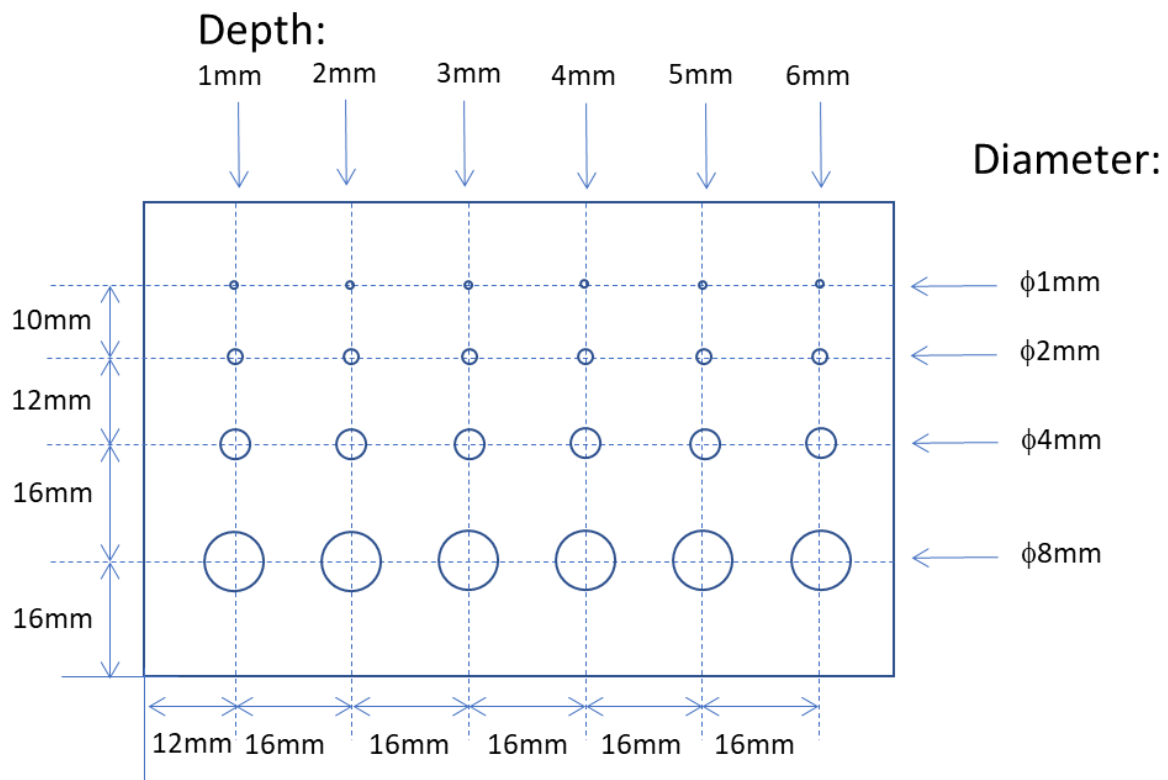


Figure 31 – Design of FBH of different diameters and depths relative to plate surface in SS304, Ni200, and C276 plates



Figure 32 – Photograph of FBH pattern in C276 plate

3.2.2. PTT imaging of Stainless Steel 304 plate with flat bottom holes

Stainless steel 304 (SS304), which has lower corrosion is frequently used for manufacturing components outside of the reactor pressure vessel, such as piping [17]. Transmission of flash light pulse through 9.45mm (0.37in) thick SS304 plate determined that $\alpha=3.89\text{mm}^2/\text{s}$. This number is fairly close to the literature value of $\alpha=3.237\text{mm}^2/\text{s}$ [18]. Because of similar values of thermal diffusivity of SS316 and SS304, the quality of reconstructed PTT images is expected to be comparable.

Figure 33 shows reconstructions of FBH at smaller depths in the SS304 plate. Left panel of Figure 33 shows the imaged area of the plate. Right panel shows parallel plane slices reconstructions at 1mm, 2mm, and 3mm depths. The smallest FBH with 1mm diameter can be seen in both 1mm and 2mm depth plane slices. Vertical plane cross-section reconstructions similar to those presented in Section 4 were obtained for SS304 plate, but are not presented in this report.

Figure 34 shows reconstructions of FBH at larger depth in the SS304 plate. Left panel shows the imaged area. The right panel shows reconstructed parallel plane slices at 4mm, 5mm and 6mm depth. The FBH with diameters 4mm and 8mm can be seen in the images up to 6mm depth. However, smaller holes are difficult to distinguish.

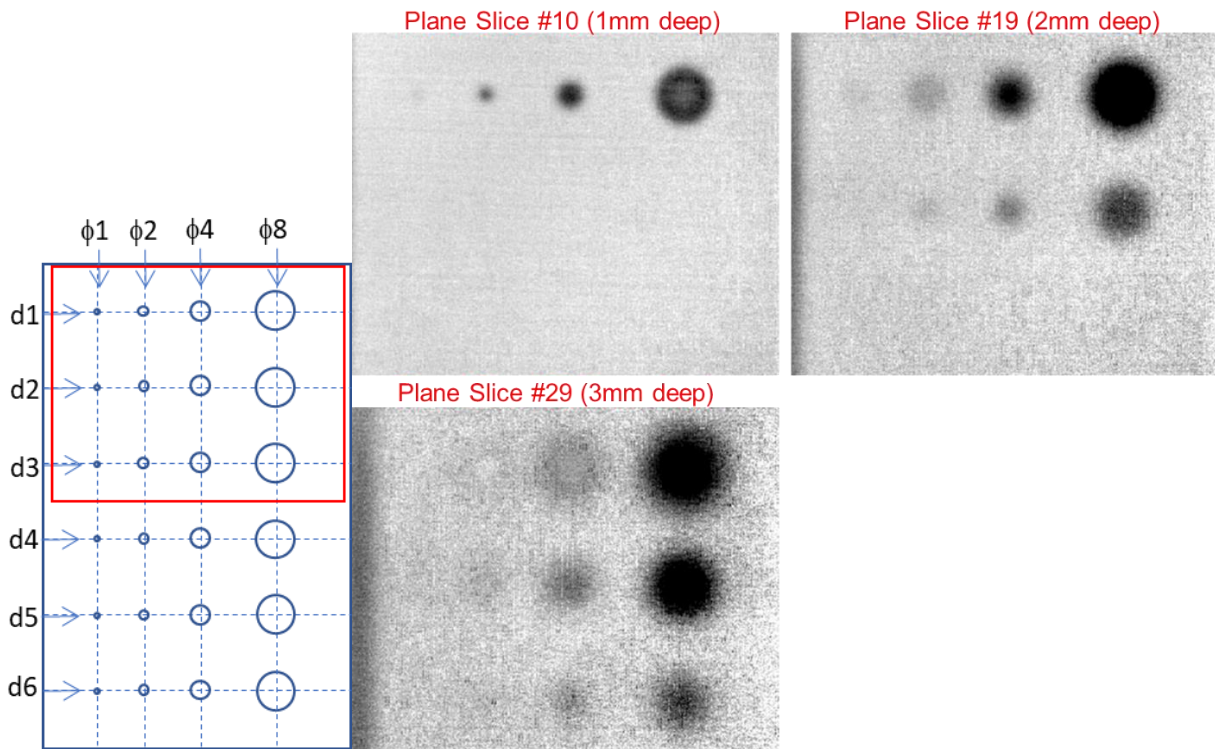


Figure 33 – Reconstruction of smaller depth FBH in SS304 plate. (Left) Imaged area. (Right) Reconstructed parallel plane slices at 1mm, 2mm, and 3mm depths.

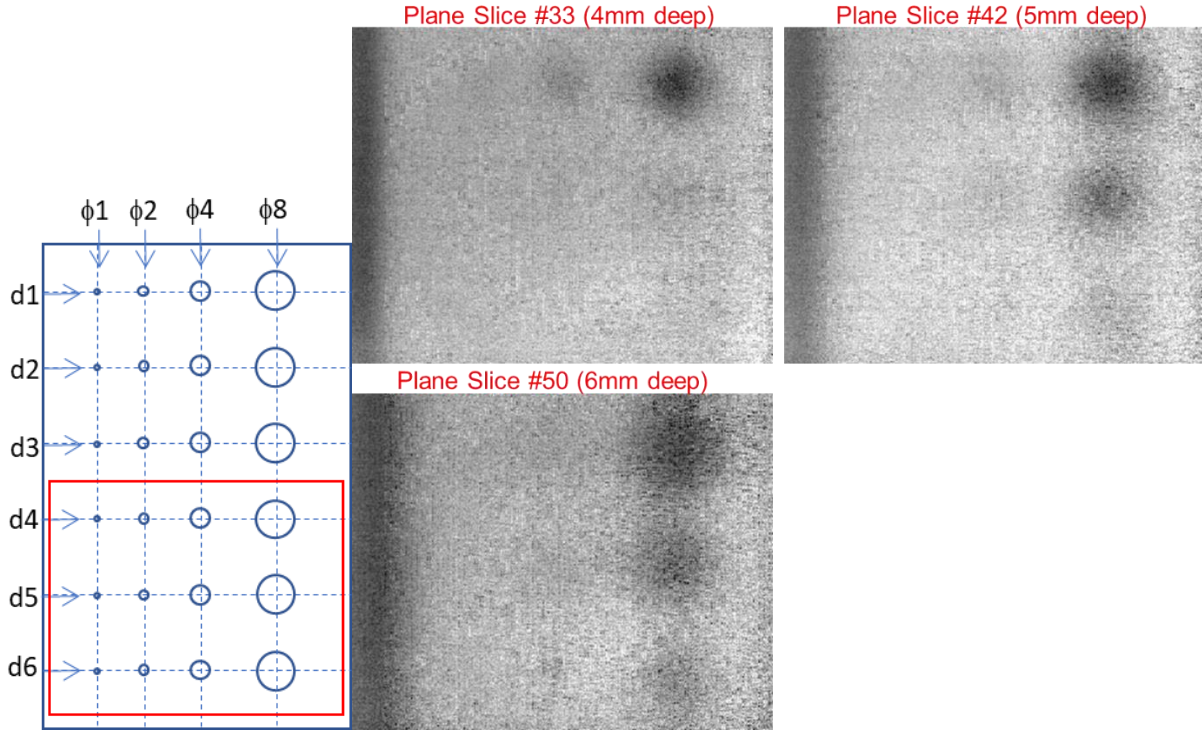


Figure 34 – Reconstruction of larger depth FBH in SS304 plate. (Left) Imaged area. (Right) Reconstructed parallel plane slices at 4mm, 5mm, and 6mm depths

3.2.3. PTT imaging of Nickel 200 plate with flat bottom holes

Nickel 200 (NI200) is a lower strength alloy than IN718. As a result, NI200 is used less frequently in nuclear applications. In this project, PTT of NI200 is investigated for comparison of reconstruction with other alloys. Transmission measurement of thermal pulse through 10.08mm (0.4in) NI200 was used to determine thermal diffusivity $\alpha=20.69\text{mm}^2/\text{s}$. This is a much higher value than those of SS316, SS304 and NI718. Therefore, reconstruction quality at greater depth is expected to be better for NI200 compared to other alloys.

Figure 35 shows reconstructions of smaller depth FBH in the NI200 plate. The left panel of Figure 35 shows the area of the plate which was imaged. The right panel shows reconstructed parallel plane slices at 1.3mm, 2mm, and 3mm depths. The FBH with 2mm diameter are clearly visible at all depths. However, the smallest FBH with 1mm diameter is difficult to detect in the plane slice images. This finding is not consistent with relatively high contrast of observed for 2mm-diameter FBH, and needs to be studies further during next quarter of the project.

Figure 36 shows reconstructions of larger depth FBH in NI200 plate. The left plane of the figure shows the imaged area of the plate. The right plane shows reconstructed parallel plane slices at 4mm, 5mm and 6mm depths. FBH with 4mm and 8mm diameters can be seen at all depths. FBH with 2mm diameter has a faint signature in the 4mm-depth plane slice. Smaller FBH are difficult to observe in the images.

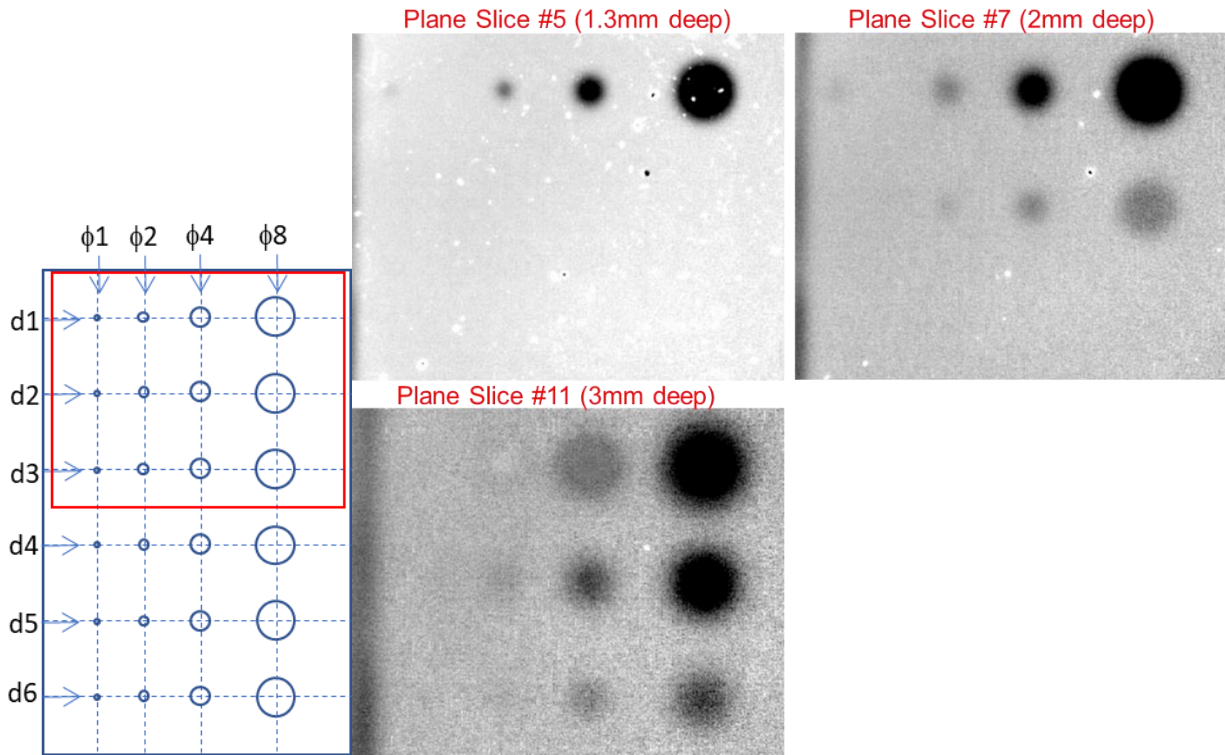


Figure 35 – Reconstruction of smaller depth FBH in NI200 plate. (Left) Imaged area. (Right) Reconstructed parallel plane slices at 1.3mm, 2mm, and 3mm depths

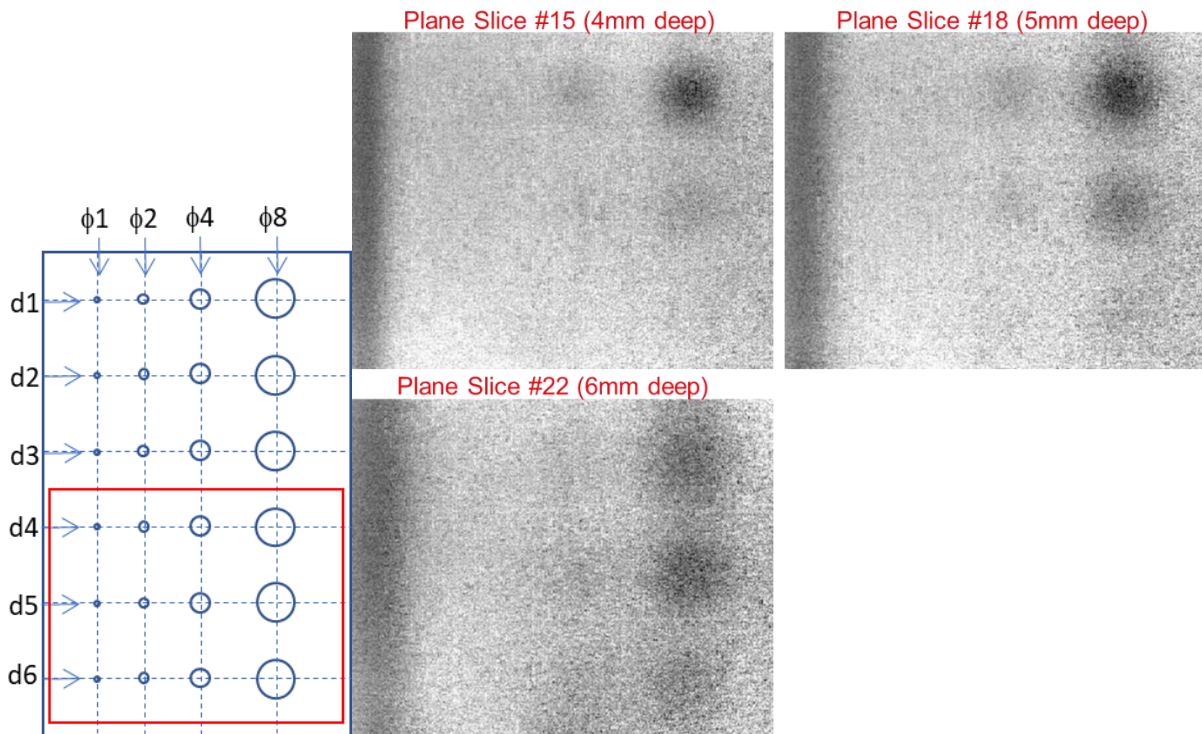


Figure 36 – Reconstruction of larger depth FBH in NI200 plate. (Left) Imaged area. (Right) Reconstructed parallel plane slices at 4mm, 5mm, and 6mm depths

3.2.4. PTT imaging of Hastelloy C276 plate with flat bottom holes

Hastelloy C276 is a high-temperature alloy frequently used for manufacturing high-temperature molten salt reactor components. Transmission of thermal pulse through 6.65mm thick C265 plate was used to determine thermal diffusivity $\alpha=2.67\text{mm}^2/\text{s}$. This value is smaller than those of SS316, SS304 and NI200, and comparable to that of IN718. Therefore, quality of reconstructed images is expected to be similar to those of the IN718 plate reconstructions.

Figure 37 shows reconstructions of parallel plane slices of smaller depth FBH. The left panel shows the imaged area of the plate. The right plane shows reconstructed parallel plane slices at 1mm, 2mm and 3mm depths. The smallest FBH with 1mm diameter is clearly visible in 1mm depth plane slice, and weakly visible in 2mm depth slice. The 2mm and 4mm diameter FBH are visible in the 3mm depth plane slice. High-contrast images of small FBH in C276 are not completely consistent with the small value of thermal diffusion, and needs to be investigated further.

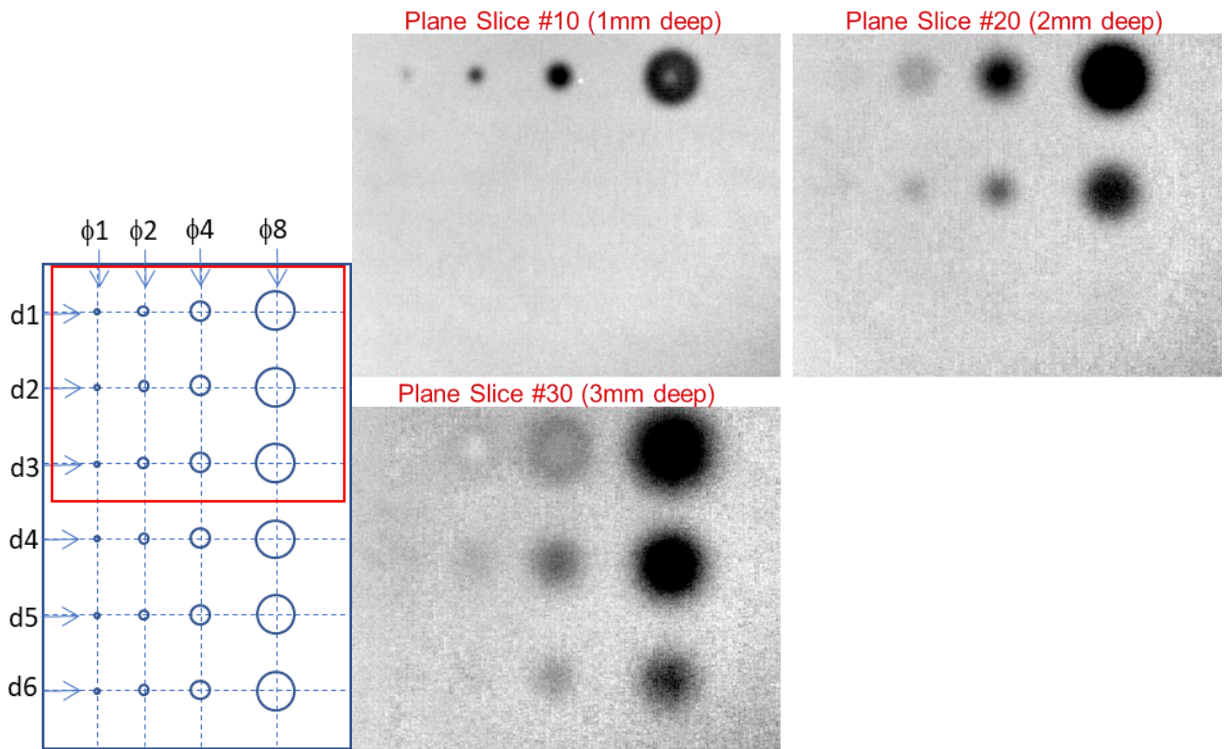


Figure 37 – Reconstruction of smaller depth FBH in C276 plate. (Left) Imaged area (Right) Reconstructed parallel plane slices at 1mm, 2mm, and 3mm depths

Figure 38 shows parallel plane slices of larger depth FBH in C276 plate. The left plane of the figure shows the imaged area of the plate. The right plane of the figure shows reconstructions of parallel plane slices at 4mm, 5mm, and 6mm depths. The FBH's with 4mm and 8mm diameters are visible in the in the plane slices at 4mm and 5mm depths, while no information can be obtained from the plane slice at 6mm depth.

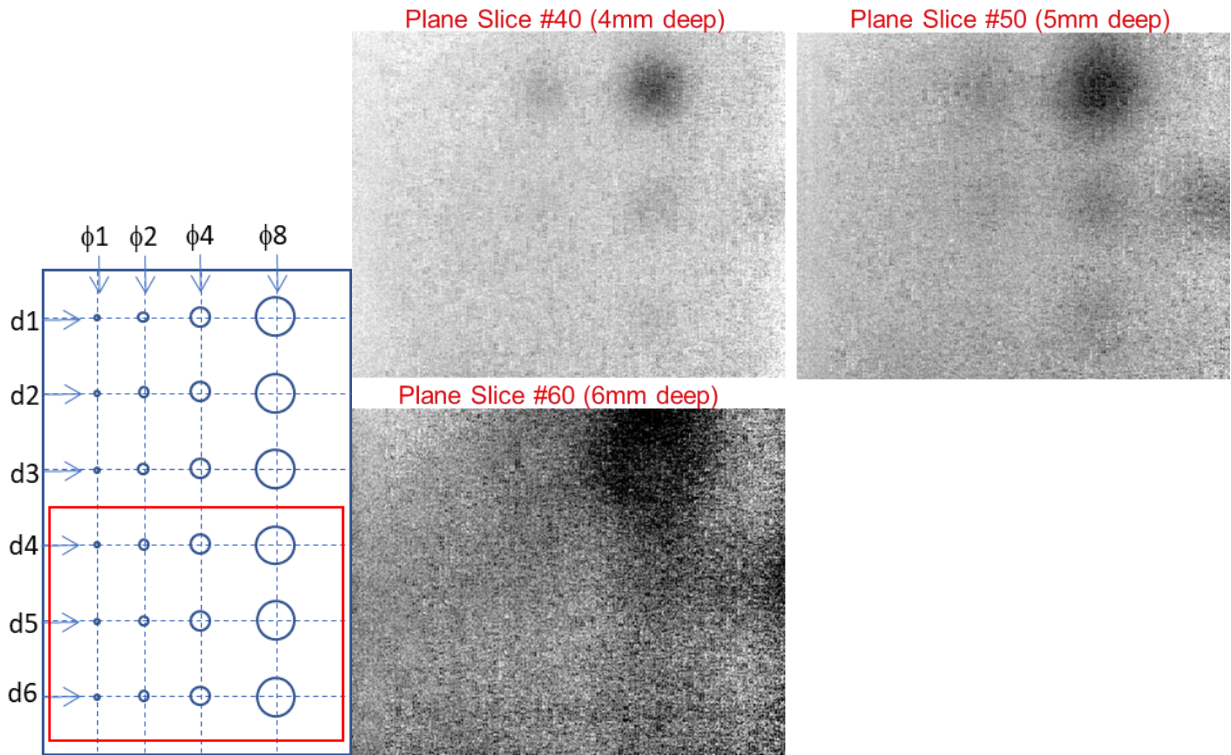


Figure 38 – Reconstruction of larger depth FBH in C276 plate. (Left) Imaged area (Right) Reconstructed parallel plane slices at 4mm, 5mm, and 6mm depths

4. Imaging of Additively Manufactured Structures with Complex Geometry

Imaging of representative AM structures was performed to investigate optimal PTT settings and evaluate system performance.

4.1. Pulsed Thermal Tomography system upgrade

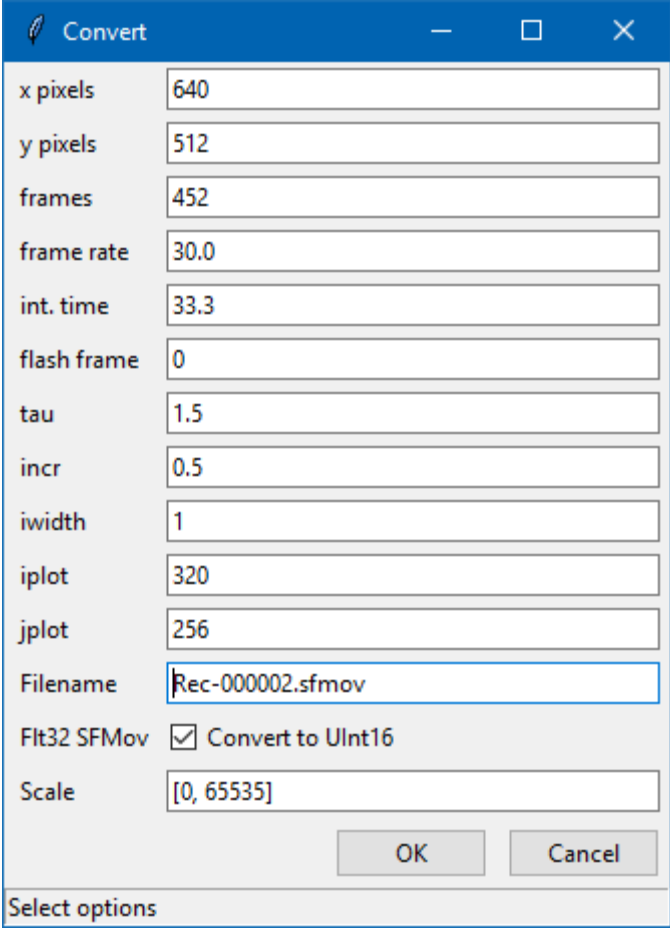
To extend the capabilities of imaging AM metallic components, hardware and software of the laboratory PTT system was upgraded through supplemental equipment funding grant provided by Argonne National Laboratory. Hardware update consists of acquiring a new FLIR X8500sc mid-wave infrared (MWIR) imaging camera, operating in 3-5 μ m band with noise equivalent temperature difference (NETD) of 20mK. X8500sc model provides maximum spatial resolution of 1280x1024, with frame rate at full window of 181Hz. The frame rate can be increased at the expense of reducing the viewing window, or equivalently reducing spatial resolution of the image. These performance parameters are superior to those of FLIR SC4000 MWIR camera used in previous generation PTT system are 320x256 spatial resolution with frame rate at full window of 420Hz and NETD of 25mK. Based on preliminary sensitivity considerations, higher spatial resolution and lower detection threshold of the new camera are expected to provide higher sensitivity in detection of flaws in AM specimens. Several configurations of the X8500sc camera (resolution, integration time and corresponding frame rate) were evaluated in imaging of flat bottom hole specimens. Parameter values of X8500sc camera used in performance evaluation are shown in Table 1. Qualitative results indicate that camera settings with spatial resolution of 768x520 pixels with 216Hz frame rate (4.6ms integration time). These are shown in boldface in Table 2.

Table 2 – Parameters of X8500sc camera

Resolution	Integration Time (ms)	Frame Rate (Hz)
320x256	5	200
640x480	4.6	216
704x512	4.1	243
768x520	4.6	216
1280x1024	5.5	181

Integration of the new camera into PTT setup required upgrading software tools for file format conversion and compatibility. In particular, interfacing with X8500sc camera is performed through FLIR Research IRTM software package, while the older SC4000 camera is controlled with FLIR Examine IRTM software package. The former software suit is not compatible with X8500sc camera. The challenge with using Research IR software package consisted of file compatibility with ANL effusivity reconstruction algorithm software. In the legacy Examine IR code, output files were generated in SFMOV format, which were converted with MATLAB script to a format

readable by the effusivity reconstruction algorithm. Research IR can be used to convert the SEQ files created by the new X8500sc camera to SFMOV files. However, it exports the SFMOV files in a floating point format, but the legacy ANL code only supports the UInt16 format. The conversion algorithm, written in Python, reads the header of the exported SFMOV file to determine the data type (encoding) of the file and read various parameters needed for analysis. Since the legacy ANL code only supports data with UInt16 encoding, the program offers the user the option to convert the file if it is encoded in any other format. Furthermore, since the values of (signed) floating point data no longer match values of unsigned integer data, the script also rescales the data to fit the full UInt16 range by default, with an option for the user to select an alternate scaling range. The program then writes the file with modified headers to indicate UInt16. Finally, the program creates and executes batch files to call the legacy code with the appropriate parameters to perform the analysis. The graphical user interface (GUI) developed for file format conversion is displayed in Figure 39.



The screenshot shows a Windows-style dialog box titled "Convert". It contains several input fields for conversion parameters:

Parameter	Value
x pixels	640
y pixels	512
frames	452
frame rate	30.0
int. time	33.3
flash frame	0
tau	1.5
incr	0.5
iwidth	1
iplot	320
jplot	256
Filename	Rec-000002.sfmov
Flt32 SFMOV	<input checked="" type="checkbox"/> Convert to UInt16
Scale	[0, 65535]

At the bottom right are "OK" and "Cancel" buttons. At the bottom left is a label "Select options".

Figure 39 – Screenshot of GUI for converting output of Research IR software to match file requirements of effusivity reconstruction code

4.2. Imaging additively manufactured IN718 nozzle plate

Additively manufactured nozzle plate, fabricated by Westinghouse using IN718 feedstock was imaged with the new PTT system. The plate is 17mm (2/3in) thick with approximately 8in by 8in cross-section. The nozzle plate was imaged with 768x520 array of pixels with 216Hz frame rate (4.6ms integration time per frame). A photograph of the PTT laboratory system for imaging of the nozzle plate with the new X8500sc camera integrated into the setup is shown in Figure 40. For better absorption of thermal energy, the imaged section of the plate was spay-painted with washable graphite paint. A photograph of the nozzle plate is shown in Figure 41(a), with highlighted section indicating area of the plate imaged with PTT is shown in Figure 41(b).

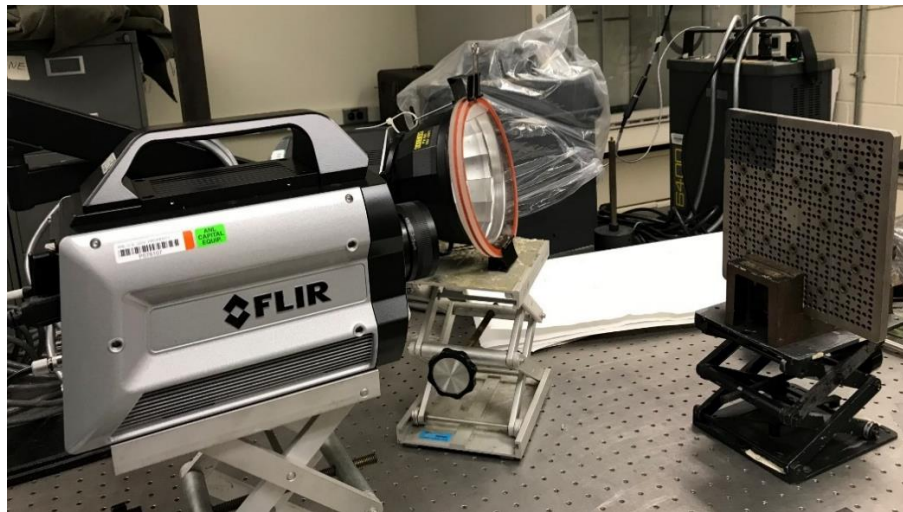
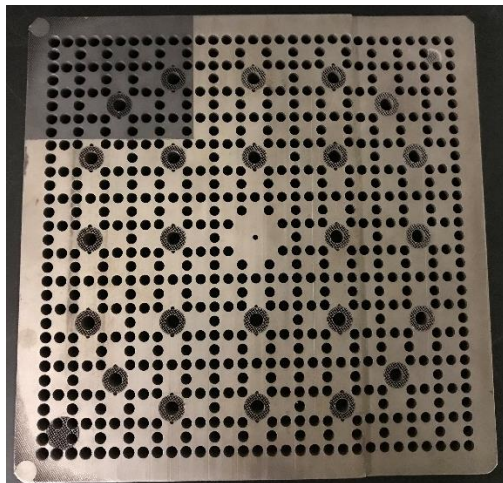
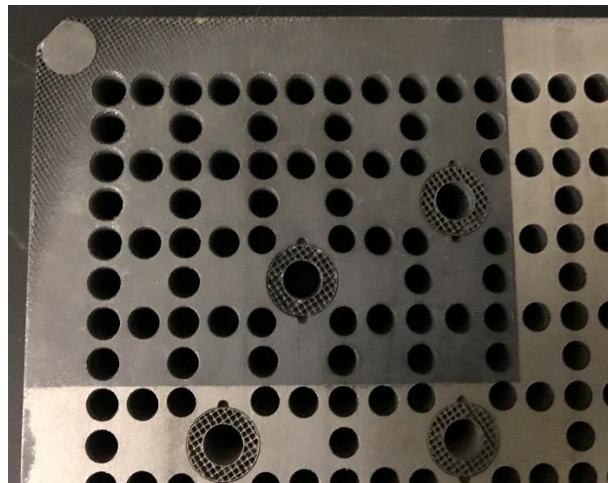


Figure 40 – Photograph of PTT setup imaging of IN718 nozzle plate with new FLIR X8500sc imaging camera



(a)



(b)

Figure 41 – (a) Photograph of the IN718 nozzle plate (b) Highlighted area imaged with PTT

Transmission measurement determined thermal diffusivity of the nozzle plate to be $\alpha=6.25\text{mm}^2/\text{s}$. This number is larger than that for solid IN718 material ($\alpha=2.82\text{mm}^2/\text{s}$) discussed in Section 4.1.3. The explanation is that the through holes in the nozzle plate result in increased thermal diffusivity of the plate structure. We use the value of $\alpha=6.25\text{mm}^2/\text{s}$ for estimating depth of reconstructed parallel plane slices. Reconstruction slices at estimated depths of 0.67mm, 1mm, 1.2mm, and 1.35mm are shown in Figure 42. The dark concentric circles in the figure correspond to spacer anchors, which are used for alignment of the plate during additive manufacturing process. The level of details in reconstructed images is significantly better than similar images obtained with SC4000 IR camera.

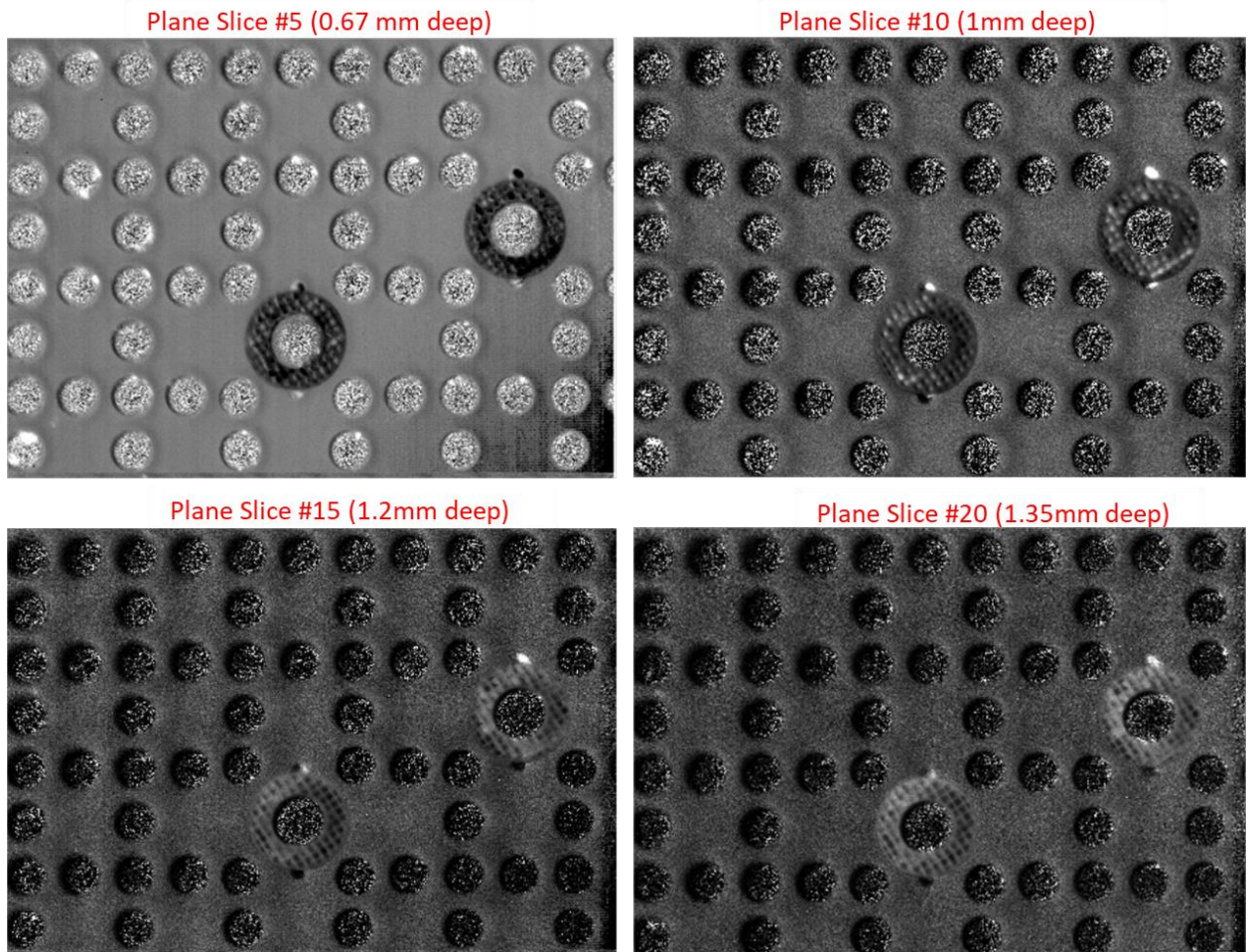


Figure 42 – Reconstruction of parallel slices of IN718 nozzle plate at 0.67mm, 1mm, 1.2mm, and 1.35mm depths

Figure 43 shows reconstructions of horizontal and vertical slices side-by-side. The left plane of the figure shows a parallel plane reconstruction at 1.35mm depth. Four horizontal lines labeled $j=20$, $j=60$, $j=142$, and $j=224$ correspond to the indices of rows of the 758×520 array of pixels in the imaging camera. Vertical cross-section plane reconstructions corresponding to lines

$j=20, 60, 142$, and 224 are shown in the right plane of Figure 43. The first image corresponding to $j=20$ line shows vertical cross-section profiles of equally spaced through-holes. The second image corresponding to $j=60$ line shows vertical cross-section profiles of a row of holes separated by a longer distance as compared to the holes in the first image. The third image corresponding to $j=142$ displays vertical and cross-sections of through-holes and a spacer at the right edge of the image. The fourth image corresponding to $j=224$ line shows vertical cross-sections of through-holes and the spacer in the middle of the image. An important feature is that front top and back surfaces of the IN718 nozzle plate are distinguishable in all images. This shows that PTT is capable of imaging through 17mm thick plate. Total imaging time was approximately 15s. Shorter imaging times resulted in cut-off view reconstructed images, while longer imaging time resulted in reconstructed images showing empty space below the back surface of the nozzle plate.

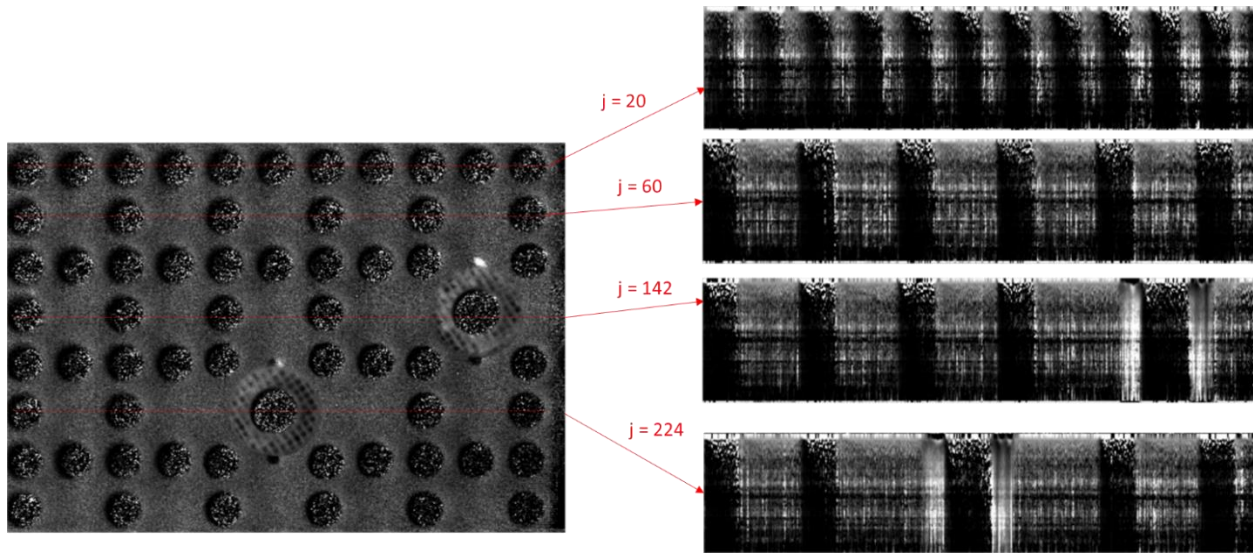


Figure 43 – Reconstruction of 3-D effusivity of IN718 nozzle plate (Left) Parallel slice at 1.35mm depth (Right) Vertical cross-section slices

Additional tasks included exploring new options for 3-D data visualization and presentation. Figure 44 shows a screen capture of ImageJ software, in which the parallel plane slices and vertical cross-sections were assembled into a 3-D viewing format. Warmer and colder colors indicate higher and lower effusivity, respectively. The cursor shown by the cross-hairs in Figure 44 allows the user to view the parallel plane slices in the main window by diving into the stack of frames. For the cursor location in the main window, the horizontal line through the parallel plane slice selects a depth-resolved cross-section plane, which can be viewed in the smaller window at the bottom window. The vertical line of the cursor in the main window selects another depth-resolved cross-section plane, which can be viewed in a smaller right window on the right. For the graphic in Figure 44, the horizontal line of the cursor cross-hairs passes through three holes and the spacer. Depth-resolved cross-section profile of these can be seen in the small window at the bottom. The vertical line of the cursor cross-hairs passes through seven holes and grazes the spacer. Depth-

resolved cross-section profile of these can be viewed in the small window on the right. The cross-hairs in the small windows at the bottom and on the right correspond to the parallel plane slice depth and horizontal/vertical position as selected by the user in the main viewing window.

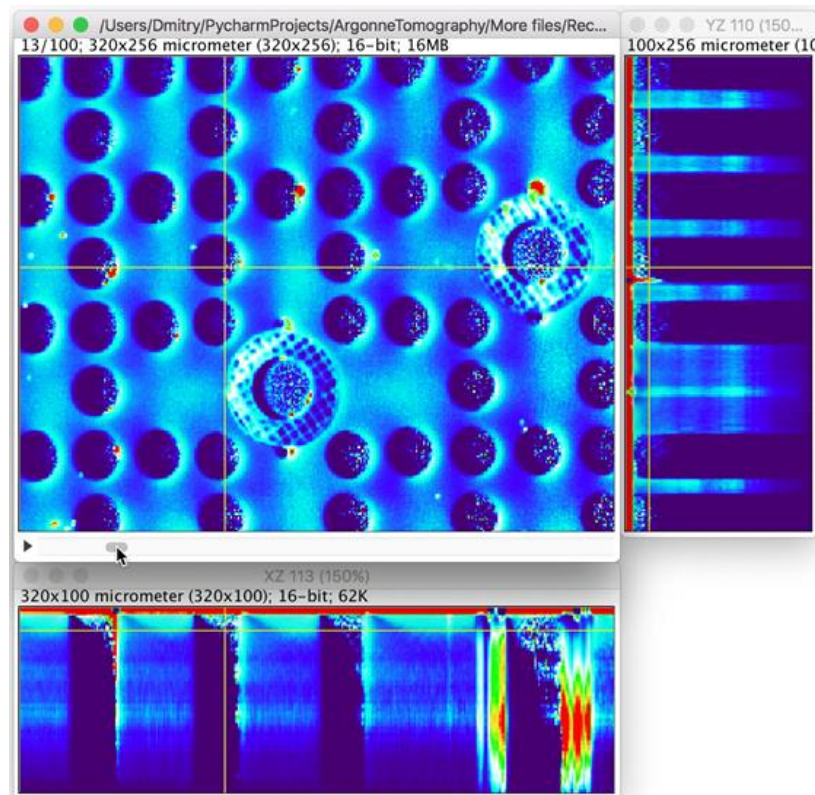


Figure 44 – Screen capture of 3-D imaging of Inconel 718 nozzle plate with ImageJ software package

Figure 45 shows another option of 3-D data visualization of the IN718 nozzle plate using MATLAB software. The 3-D data is visualized via projections on three orthogonal x-y, x-z and y-z planes. The planes can be moved independently in 3-D space by the user. Figure 45 shows one particular configuration of three orthogonal planes. Warmer and colder colors indicate higher and lower effusivity, respectively.

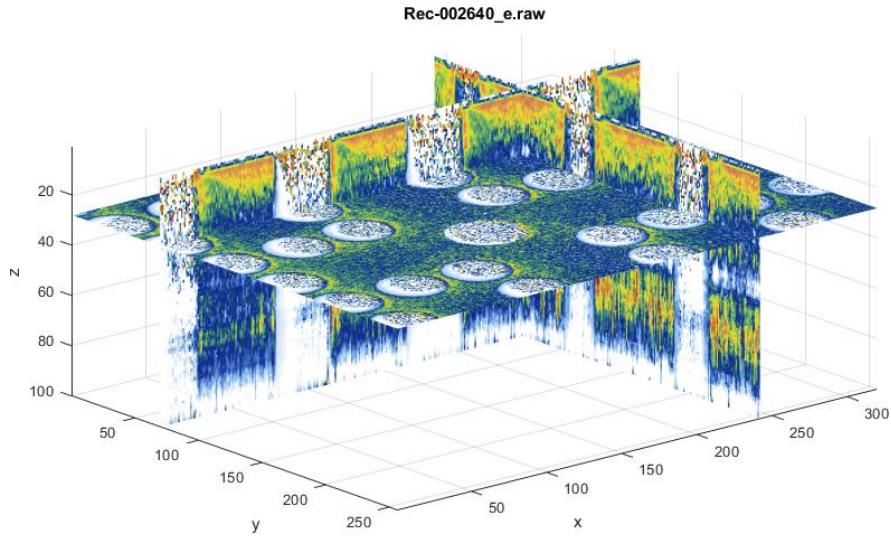


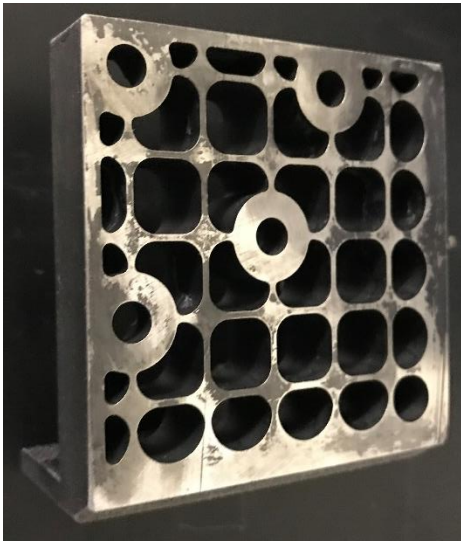
Figure 45 – 3-D imaging of NI718 nozzle plate reconstructions with MATLAB

4.3. Imaging additively manufactured IN718 particle filter plate

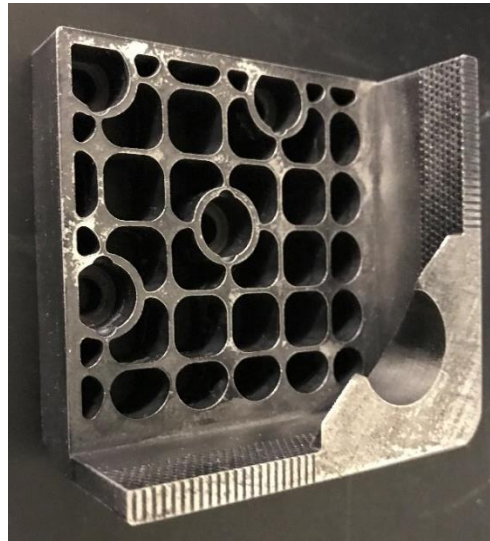
Additively manufactured particle filter plate for removing contaminations in the cooling fluid, fabricated by Westinghouse using DLS method using IN718 feedstock, was imaged with the new PTT system. A photograph of the PTT laboratory system for imaging of the nozzle plate with the new X8500sc camera integrated into the setup is shown in Figure 46. The section of the plate is approximately 3in by 3in, with approximately 0.5in base height and a side piece of total height of approximately 1.5in and 0.2in thickness. A photograph of the filter plate is shown in Figure 47, where Figure 47(a) displays the top view, and Figure 47(b) displays the bottom/side view. The plate contains a number of through-penetrations, which in an actual filter plate would contain wires for trapping small particles, which are not part of the article in the imaging study. The nozzle plate was imaged with 768x520 array of pixels with 216Hz frame rate (4.6ms integration time per frame).



Figure 46 – Photograph of PTT laboratory setup for imaging of IN718 particle filter plate with new FLIR X8500sc imaging camera



(a)



(b)

Figure 47 – Photograph of the filter plate (a) top view (b) bottom/side view

Because of the presence of large number of through-penetrations, thermal diffusivity of the filter plate is the same as that of the nozzle plate, $\alpha=6.25\text{mm}^2/\text{s}$. This value was used for depth estimation of reconstructions. The filter plate was first imaged through the top surface, shown in Figure 47(a). Parallel plane reconstruction slices at estimated depths of 1mm, 1.35mm, 1.65mm, and 1.9mm are shown in Figure 48.

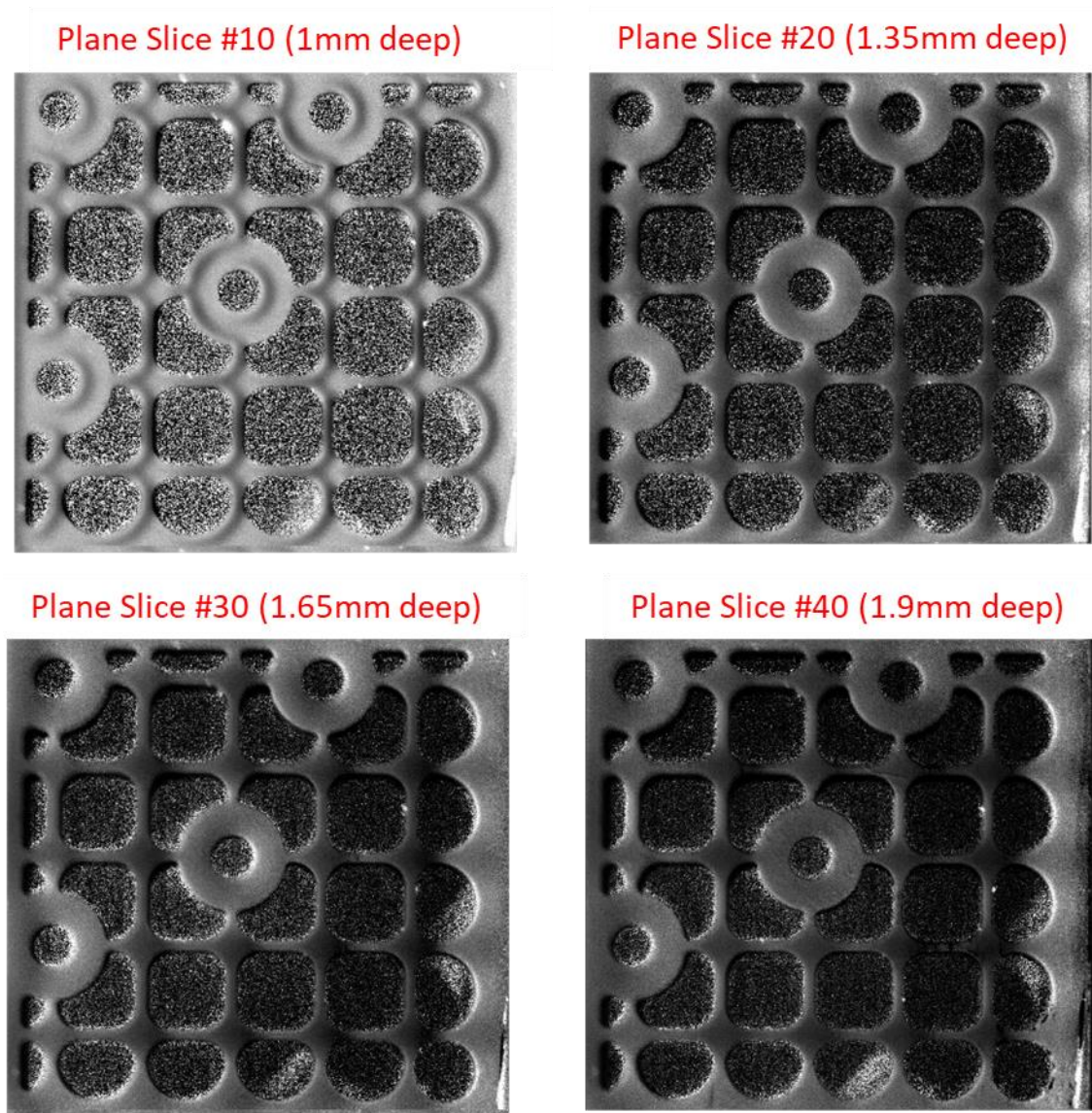


Figure 48 – Reconstruction of parallel slices of IN718 particle filter plate top face at estimated 1mm, 1.35mm, 1.65mm, and 1.9mm depths

Figure 49 shows reconstructions of horizontal and vertical slices side-by-side. The left plane of the figure shows a parallel plane reconstruction at 1.9mm depth. Four horizontal lines labeled $j=14$, $j=45$, $j=56$, and $j=170$ correspond to the indices of rows of the 758×520 array of pixels in the imaging camera. Vertical cross-section plane reconstructions corresponding to lines $j=14, 45, 56$, and 170 are shown in the right plane of Figure 49. The first image corresponding to $j=14$ line shows vertical cross-section profiles near the edge of the plate. The second image corresponding to $j=45$ line shows vertical cross-section profiles of a section of the plate drawn mostly through solid material. The third image corresponding to $j=56$ displays vertical and cross-sections of reconstructions of several through-holes. The fourth image corresponding to $j=170$ line shows vertical cross-sections of through-holes. As in the case of the nozzle plate, an important feature is

that front top and back surfaces of the IN718 particle filter distinguishable in all images. Total imaging time was approximately 15s. Shorter imaging times resulted in cut-off view reconstructed images, while longer imaging time resulted in reconstructed images showing empty space below the back surface of the nozzle plate.

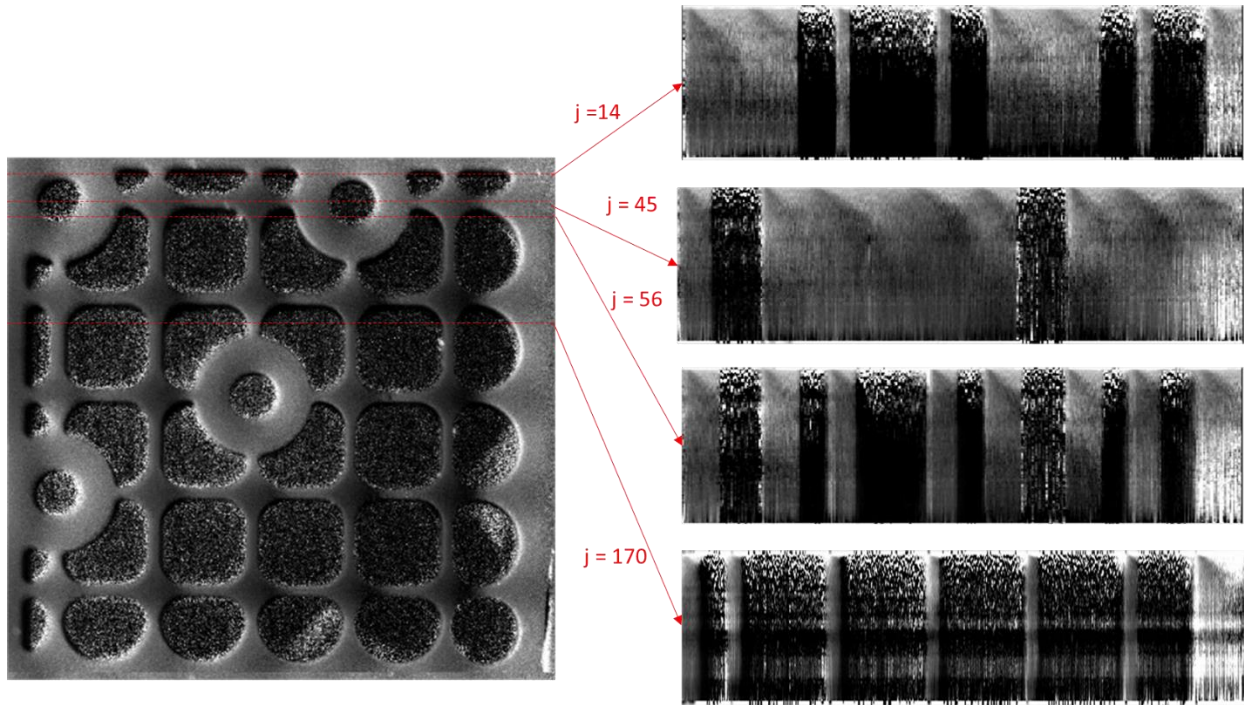


Figure 49 – Reconstruction of 3-D effusivity of IN718 filter plate (Left) Parallel slice at 1.9mm depth (Right) Vertical cross-section slices

Next, the particle filter plate was imaged through the solid side surface, as seen in Figure 47(b). For heat diffusion through mostly solid IN718, thermal diffusivity is $\alpha=2.82\text{mm}^2/\text{s}$. Parallel plane reconstruction slices at estimated depths of 0.75mm, 0.9mm, 1.1mm, and 1.3mm are shown in Figure 50. Note that relevant information is contained only in the bottom and right side parts of the figure. The side section of the plate is approximately 3mm thick. The images in Figure 50 are complimentary to those in the vertical cross-sections in the right panel of Figure 49, particularly reconstructions corresponding to $j=14$ near the edge of the plate. Dark regions at the bottom of images appearing in reconstructions corresponding to greater depth in Figure 50 indicate through-holes in the filter plate.

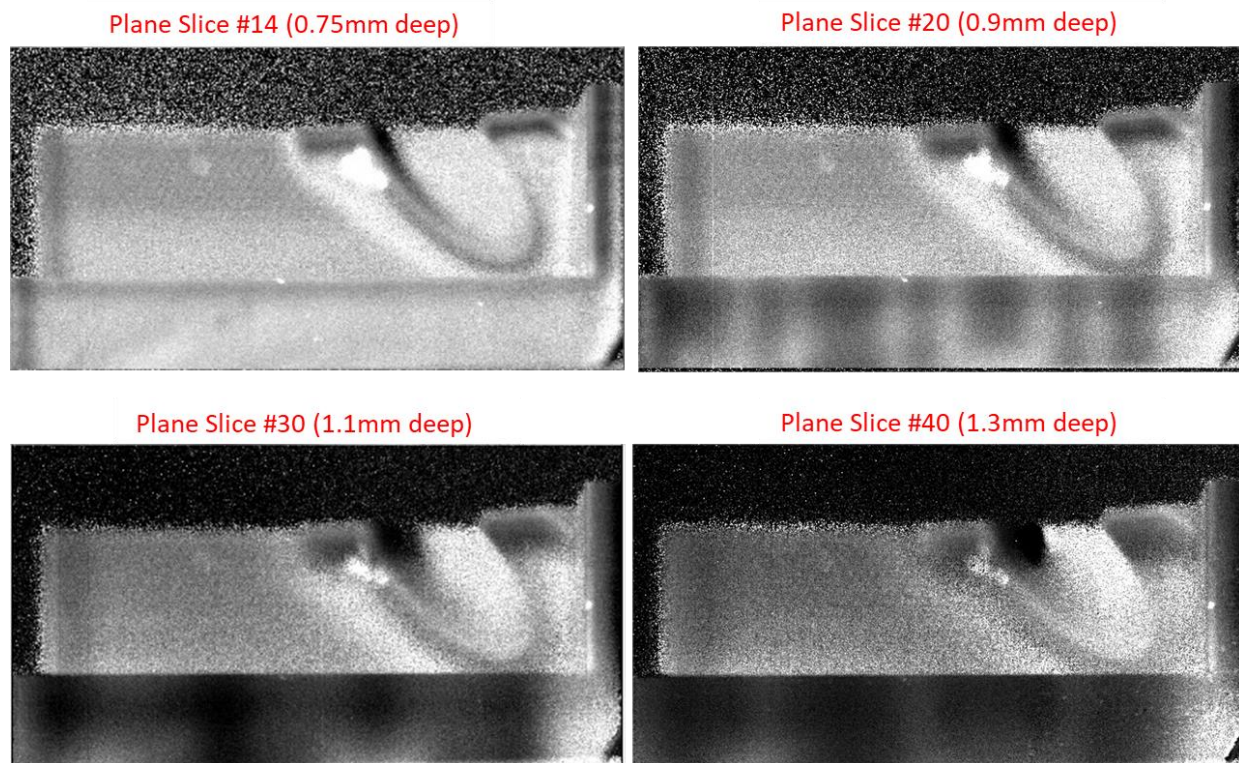


Figure 50 – Reconstruction of parallel slices of IN718 particle filter plate side face at estimated 0.75mm, 0.9mm, 1.1mm, and 1.3mm depths

5. Conclusions

The objective of this report is to provide initial evaluate pulsed thermal tomography (PTT) performance in detecting calibrated flaws in reactor structural materials using computer modeling and experiments. The limits of PTT capability in detection of defects in metallic plates were investigated using COMSOL numerical modeling of heat transfer. Defects were modeled as cylindrical flat bottom holes (FBH), which is a common model of calibrated material flaws in thermal tomography experiments. Materials considered in this study include stainless steel 316 (SS316), stainless steel 304 (SS304), and Inconel 718. Theoretical analyses were conducted to validate inversion of simulated PTT data with COMSOL for an infinite plate, for which there exists an analytical solution. Subsequently, 3D reconstructions were performed on COMSOL simulations for FBH, revealing a decrease in spatial resolution over depth due to thermal diffusion. The results of this study show that the performance of the inversion algorithm for detecting smaller defects depends strongly on the depth of the defect as well as the incident heat flux. The size of detectable defect was estimated by fitting a Gaussian function to surface temperature profile. The criteria for detectability was taken as 20mK noise equivalent temperature difference (NETD), which is currently the sensitivity limit of high-performance infrared cameras. It was determined through COMSOL simulations that the smallest detectable FBH in SS316 has a 50 μ m diameter and is located 0.5mm below the plate surface

In the experimental studies, high strength Stainless Steel 316 and Inconel 718 alloys were considered, as well as lower grade Stainless Steel 304, Nickel 200, and Hastelloy C276. Specimens investigated in this report consisted of approximately 1/4in-thick plates made out of these alloys using conventional manufacturing methods. The calibrated defects were created in the form of flat bottom holes (FBH) drilled in metallic plates. The diameters of FBH's varied from 1mm to 8mm, and their depths below the plate flat surface varied between 1mm and 6mm. The size of the smallest FBH was limited to 1mm because conventional mechanic drills were used for creating the holes. PTT imaging results have shown that 1mm-diameter FBH located 1mm and 2mm below the surface were detectable. Larger size FBH were detectable at greater depth. For example, 6mm-diameter FBH could be detected at 8mm depth. Image contrast varied slightly between the specimens, with the best reconstructions obtained in SS316 and C276 plates.

The capability of PTT in imaging complex geometry AM structures was evaluated using several structures fabricated from Inconel 718 (IN718) powder feedstock. The AM structures in this study did not have calibrated internal defects. The objective is to determine PTT settings, such as the total integration time, for imaging of representative AM structures. A new FLIR X8500sc IR camera with higher spatial resolution (1280x1024 at 181Hz frame rate) was integrated into the PTT laboratory setup. Software tools were developed to ensure compatibility of new camera files with legacy effusivity reconstruction codes. The new camera was used to obtain 3-D reconstructions of IN718 nozzle plate and a particle filter plate. The results demonstrate the capability of PTT in 3-D imaging of complex geometry AM structures. Further, increased resolution imaging is achieved compared to prior results using older FLIR SC4000 IR camera. It was shown that PTT can scan through a 2/3in-thick Inconel 718 plates produced with AM method

in approximately 15s. Several modes of 3-D data visualization were explored, including using ImageJ and MATLAB software packages. Intermediate results demonstrated in this report will be developed further in detection of flaws in AM specimens.

Next phase of the project work will investigate detection of spherical-shape defects representing regions of porosity, which will be imprinted in AM specimens. In addition, detection and imaging of cracks imprinted into AM specimens will be explored. Machine learning algorithms for feature detection and extraction will be studied in parallel [19]. Further studies will be conducted on evaluating PTT performance with a portable system, and performance of the portable PTT system in a prototypical in-service environment.

References

1. Bertali, G., Wang, Y., Lim, J., Scenini, F., Long, C., Freyer, P., and Burke M., "Microstructural Analysis of 3D-Printed Alloy 718," *Microscopy and Microanalysis*, 21(S3), 463-464 (2015).
2. Freyer, P.D., Cleary, W.T., Ruminski, E.M., Long, C.J., Xu, P., "Hot Cell Tensile Testing of Neutron Irradiated Additively Manufactured Type 316L Stainless Steel," *Proceedings of the 18th International Conference on Environmental Degradation of Materials in Nuclear Power Systems -- Water Reactors: Volume 1*, 1021-1038 (2018).
3. Cunningham, R., Narra, S. P., Montgomery, C., Beuth, J., & Rollett, A. D. (2017). Synchrotron-based X-ray microtomography characterization of the effect of processing variables on porosity formation in laser power-bed additive manufacturing of Ti-6Al-4V. *Jom*, 69(3), 479-484.
4. Zhao, C., Fezzaa, K., Cunningham, R. W., Wen, H., Carlo, F., Chen, L., & Sun, T, "Real-time monitoring of laser powder bed fusion process using high-speed X-ray imaging and diffraction," *Scientific reports*, 7(1), 3602 (2017).
5. Kempen, K., Yasa, E., Thijs, L., Kruth, J. P., & Van Humbeeck, J., Microstructure and mechanical properties of Selective Laser Melted 18Ni-300 steel. *Physics Procedia*, 12, 255-263 (2011).
6. Sames, W. J., List, F. A., Pannala, S., Dehoff, R. R., & Babu, S. S., "The metallurgy and processing science of metal additive manufacturing," *International Materials Reviews*, 61(5), 315-360 (2016).
7. Lewandowski, J. J., & Seifi, M. Metal additive manufacturing: a review of mechanical properties. *Annual Review of Materials Research*, 46, 151-186 (2016).
8. Heifetz A., Lisowski D., Weathered M., Momozaki Y., Chien H.T., Bakhtiari S., "Preliminary Review Analysis of Distributed Sensors for Versatile Test Reactor (VTR) Environment," Argonne National Laboratory, ANL/NSE-18/11 (2018).
9. Wakamatsu M., Nei H., and Hashiguchi K., "Attenuation of temperature fluctuations in thermal striping," *J. Nucl. Sci. Technol.*, vol. 32, no. 8, pp. 752-762 (1995).
10. Sun J.G., "Quantitative three-dimensional imaging of heterogeneous materials by thermal tomography," *Journal of Heat Transfer* 138, 112004. (2016).
11. Sun J.G., "Pulsed thermal imaging measurement of thermal properties for thermal barrier coatings based on a multilayer heat transfer model," *Journal of Heat Transfer* 136, 081601. (2014).
12. Heifetz A., Sun J.G., Elmer T., Shribak D., Saboriendo B., Kozak P., Bakhtiari S., Cleary W., Khaykovich B., "PTT System Performance Evaluation in 3-D Imaging of Calibrated Defects," Argonne National Laboratory, ANL-19/12 (2019).
13. Heifetz A., Liu T., Shribak D., "PTT System Design and Data Analysis for Improved Performance," Argonne National Laboratory, ANL-19/25 (2019).
14. Heifetz A., Elmer T.W., Zhang X., Saniie J., "PTT System Performance Evaluation in 3-D Imaging of AM Components," Argonne National Laboratory ANL-19/38 (2019).
15. Balageas, D. L., Krapez, J. C., and Cielo, P., "Pulsed Photothermal Modeling of Layered Materials," *J. Appl. Phys.*, 59(2), pp. 348-357 (1986).

16. Parker, W. J., Jenkins, R. J., Butler, C. P., and Abbott, G. L., "Flash Method of Determining Thermal Diffusivity, Heat Capacity, and Thermal Conductivity," *J. Appl. Phys.*, 32(9), pp. 1679–1684 (1961).
17. Kultgen D., Grandy C., Kent E., Weathered M., Andujar D., and Reavis A., "Mechanisms Engineering Test Lopp – Phase I Status Report – FY2018," Argonne National Laboratory ANL-ART-148, ANL-METL-14 (2018).
18. Kim C.S., "Thermophysical properties of stainless steels," Argonne National Laboratory ANL-75-55 (1975).
19. Luo, Q., Gao B., Woo W.L., Yang. Y., "Temporal and spatial deep learning network for infrared thermal defect detection," *NDT&E International* 108, 102164 (2019).



Nuclear Science and Engineering (NSE) Division

Argonne National Laboratory

9700 South Cass Avenue, Bldg. 208

Argonne, IL 60439

www.anl.gov



Argonne National Laboratory is a U.S. Department of Energy
laboratory managed by UChicago Argonne, LLC